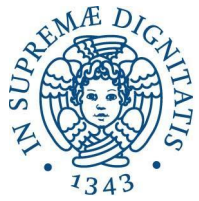

Università di Pisa

FACULTY OF AEROSPACE ENGINEERING
Master of Science degree in Space Engineering

GRADUATION THESIS

IN COLLABORATION WITH
von Karman Institute for fluid dynamics
Turbomachinery department

Measurement techniques in a transonic wind tunnel

Total Temperature and Turbulence characterization

Candidate:
Gabriele Bonucci

Advisors:
Prof. Eng. Luca d'Agostino
Prof. Eng. Guillermo Paniagua
Eng. Laura Villafañe

Academic Year 2012-2013

To my grandmother.

Abstract

Novel technologies on high-bypass ratio engines are being developed to improve their performances. New architectures tend to increase the engine's oil circuit cooling demand. A new refrigeration solution is the main objective of the Intelligent Cooling System project.

This study is based on a surface integrated air-oil heat exchanger placed at the location of the air separator nose within the bypass flow of a turbofan. The aim is to help the cooling of the oil circuit without disturbing the air stream and decreasing the overall efficiency of the engine.

The present work focuses on the aerodynamic characterization of the interaction between the three dimensional bypass flow and different configurations of finned heat exchangers. This research is done in von Karman Institute (VKI) in a new blowdown wind tunnel characterized by an helicoidal test section specifically designed within this project in order to reproduce the engine bypass flow in the region of interest.

Different measurement techniques were employed for the aerodynamic characterization. This report presents the work performed for the calibration and implementation of some of the measurement techniques as well as part of the flow results.

Particular attention was given to temperature and turbulence measures, emphasizing the way of functioning of the measurement devices and the postprocessing methodology.

Finally the uncertainties analysis was done in order to estimate the goodness of the results and to identify the major sources of errors.

This work achievements help the characterization of the investigated finned heat exchangers.

Acknowledgments

I would express my gratitude first of all to von Karman Institute (VKI) and all its member for the new and challenging working environment that I discovered, but also for the possibility to meet a lot of great colleagues and new friends.

My sincere thanks goes to my advisor Laura Villafañe for her continuous support, her advises, and for all the time that she gave me to correct my errors and to teach me most part of what I learned.

Thanks go to my supervisor professor Paniagua first of all for his precious hints, but also to let me feel part of his working team.

I would thank also Daniele Massini and Fabrizio Fontaneto for their help and mostly for the funny sketches that make my hard laboratory days more tolerable. In this I cannot forget Pierre Londers, the craziest and most amusing technician that I have ever known.

A special thank goes to my parents and my girlfriend Elisa for the emotive support that they gave me in my first experience in a foreign country, without them I never finished my stage and my thesis and I never enjoyed this working period. All their visits recharge me and allow me to reach the end of my work.

Finally thanks to all the 2011-2012 research master students and all the other stagers that I met, thanks for all the beautiful days that I lived with them.

This work was carried out in the frame of the *INTELLIGENT COOLING SYSTEM* project. The author would like to acknowledge the financial support of the *Region Wallone*, the pole of competitiveness *Skywin*, and the industrial support of *TechSpace Aero*.

Contents

List of Figures **ix**

List of Tables **xi**

List of Symbols **xiv**

List of Acronyms **xiv**

1 Introduction **1**

1.1 Introduction 1

1.1.1 Environmental Impact 3

1.1.2 Performance 6

1.2 Experimental setup 8

1.2.1 Wind Tunnel characteristics 8

1.2.2 Measurement planes 10

I Measurement background **16**

2 Temperature measurements **17**

2.1 Probe description 17

2.2 Measurement chain 19

2.3 Calibration 20

2.3.1 Oven calibration details 20

2.3.2 Noise tests 21

2.4 Buffer memory test 24

3 Pressure measurements **27**
3.1 Total pressure measurement 27
3.2 Static pressure measurement 29
3.3 Five holes probe 29

4 Hot Wire Anemometry measurements **31**
4.1 Introduction 31
4.2 Constant Temperature Anemometry 32
4.3 Probe 34
4.4 Calibration 41
4.4.1 Square wave test 42
4.4.2 Calibration facility 43
4.5 Angle sensitivity analysis 44
4.6 Conclusion 46

II Experimental investigation **48**

5 Flow analysis **49**
5.1 Total Temperature 49
5.1.1 Mapping procedure 49
5.1.2 Plane 2, 3 and 4 maps 50
5.1.3 Noise analysis 55
5.2 Turbulence 63
5.2.1 Mapping 64
5.2.2 Frequency content analysis 70
5.3 Conclusion 72

6 Uncertainties analysis **74**
6.1 Temperature ratio uncertainty 74
6.2 Turbulence uncertainty 75
6.2.1 Velocity uncertainty 76
6.3 Conclusion 77

III Conclusion **79**

7 Conclusion and further investigations **80**

7.1 Conclusion 80
7.2 Future works 81

A Matlab codes **83**
A.1 Real Over Heat Ratio (OHR) 83
A.2 Total temperature uncertainty 84
A.2.1 Code 84
A.3 Turbulence uncertainty 87

References **90**

List of Figures

1.1 Thrust efficiency versus $\frac{v_e}{v}$. 3
1.2 Thrust efficiency in function of upstream asymptotic air speed. 4
1.3 Comparative noise levels of various engine types. 5
1.4 Position of the heat exchanger and direction of the fins. . . . 7
1.5 Heat exchanger location and research domain. 8
1.6 Wind tunnel sketch. 9
1.7 Geometry of the five measure planes along wind tunnel. . . . 11
1.8 Plane 5 measurement grids examples. 14
1.9 Angle of immersion δ of the Shielded Thermocouple type T (STT) probe rake. 14
1.10 Picture of the test section. 15
1.11 Tested heat exchanger configurations. 15

2.1 Thermocouple examples. 18
2.2 Temperature reference unit. 19
2.3 Envelope used in the oven calibration. 21
2.4 Signal deriving from amplifier channel 6. 25
2.5 Signal deriving from amplifier channel 11. 26

3.1 Pressure scanner. 27
3.2 Pitot tubes rake sketch. 28
3.3 Static pressure taps position. 29
3.4 Five holes rake sketch. 30

4.1 Typical anemometric system. 33

4.2 Schematic control circuit for CTA. 35
4.3 Control circuit for CTA, considering the cabling influence. . . 35
4.4 Hot-Wire probe drawing. 36
4.5 VKI made Hot-Wire CTA control circuit. 38
4.6 Dantec Hot-Wire CTA control circuit. 39
4.7 National Instrument USB-6255. 40
4.8 Control circuit answers to a square wave input. 43
4.9 Head 3: example of square wave test result. 44
4.10 Schematic view of calibration facility. 44
4.11 Hot wire angular regulator. 45
4.12 Scheme of pitch and yaw angles. 45
4.13 Hot wire 6 calibration curve, data at different pitch angles and effective velocity values. 47

5.1 Plane 2 measurement points and triangulation mesh. 50
5.2 Plane 2 non-dimensional total temperature map with continuous fin heat exchanger. 51
5.3 Plane 3 non-dimensional total temperature maps. 52
5.4 Plane 4 non-dimensional total temperature maps. 53
5.5 Plane 4 non-dimensional total temperature maps in the central zone with fine grid. 54
5.6 STT2 noise level in plane 4 with continuous fin configuration. 56
5.7 STT2 noise level during calibration. 57
5.8 STT2 noise level in plane 4 with continuous fin configuration after filtering. 58
5.9 STT6 noise level in plane 4. 60
5.10 STT6 noise level during calibration. 61
5.11 STT6 noise level in plane 4. 62
5.12 Plane 3 turbulence intensity (clean configuration). 64
5.13 Plane 4 turbulence map comparison (coarse grids). 66
5.14 Plane 4 turbulence intensity map with the interrupted fin heat exchanger (coarse map). 67
5.15 Plane 4 continuous fin configuration turbulence maps details. 68
5.16 Plane 5 turbulence map comparison (central part of the section). 69
5.17 Typical power spectral density (plane 4 interrupted fin configuration). 71

5.18 Plane 4 map in the interrupted fin configuration digital filtered, with cutting frequency at 30 kHz. 72

6.1 Main velocity uncertainty sources in the case of hot wire 5. . 76
6.2 Total velocity uncertainty in the case of hot wire number 5. . 77
6.3 Turbulence relative uncertainty. 78

List of Tables

1.1 Angle of immersion per each measurement plane. 13

2.1 Type T thermocouple characteristics 17
2.2 Characteristic slope and offset of used STT 21
2.3 Gain of each type T amplifier channels 22
2.4 Noise of each channel at T_{amb} without filtering. 23

4.1 Sensing wire characteristics. 37
4.2 Wire cold resistances. 37
4.3 Support resistances. 37
4.4 Over Heat Ratios. 39
4.5 Unified BNC cables details. 40
4.6 Hot Wire probe dimensional calibration. 42
4.7 Dimensional calibration R^2. 42
4.8 Limiting answer frequency. 43

5.1 Noise during calibration and tests of STT2 (the reference test is plane 4 continuous fin configuration). 55
5.2 Noise during calibration and tests of STT6 (the reference test is plane 4 continuous fin configuration). 59
5.3 Noise during calibration and tests for the other probes without filtering. The reference test is plane 4 continuous fin configuration for head number 1, 4 and 5, while plane 4 continuous fins bis for the STT0 and finally plane 4 interrupted fins for the STT7). 63

5.4 Mean turbulence level in plane 4 for different configurations. . 67
5.5 Hot Wire rake head filter cutoff frequency. 70

List of Symbols

T	Thrust, temperature	[N], [°C]
m	Mass	[kg]
v	Velocity	[m/s]
A	Area	[m^2]
p	Pressure	[N/m^2]
KE	Kinetics energy per unit time	[W]
η	Efficiency	
P	Power	[W]
f	Fuel/air mass flow rate ratio, function of, non dimensional temperature ratio	
δ	Probe angle of immersion, uncertainty	[deg],[any]
ω	Resonance frequency	[Hz]
R	Resistance	[Ω]
H	Correlation function	
E	Output voltage	[V]
M	Time constant	[s]
K	Amplifier gain	
L	Inductance	[H]
Δ	Interval	
α	Wire resistivity, pitch angle	[1/K], [deg]
V	Voltage	[V]
u	Velocity	[m/s]
Re	Reynolds number	
Nu	Nusselt number	
f_{MAX}	Maximum frequency	[Hz]

τ	Square wave test time constant	[s]
θ	Yaw angle	[deg]
Tu	Turbulence	
σ	standard deviation	[any]

Subscripts

e	Exit quantity
i	Inlet quantity
T	Thrust, total quantity
mec	Mechanical
th	Termodynamical
o	Overall
f	Fan flow
c	Core flow, cutoff
w	Wire
0	Ambient
1	Relative to the electronic circuit
TOT	Total
eff	Effective
ref	Relative to reference probe
u	Relative to velocity

Special symbols

$\dot{}$	Time derivative
∂	Partial derivative
d	Total derivative

Acronyms

ACOC Air Cooled Oil Cooler

BPR Bypass Ratio

CCA Constant Current Anemometry

CFD Computational Fluid Dynamics

CO Carbon Monoxide

CO_2 Carbon Dioxide

CTA Constant Temperature Anemometry

CV Coefficient of Variation

Measure of dispersion of data relative to the mean. It is defined as the standard deviation divided by the mean.

CVA Constant Voltage Anemometry

DAS Data Acquisition System

EPNdB Effective Perceived Noise decibel

A complex rating used to certify aircraft types for flyover noise, based on the sound pressure. Includes corrections for pure tones and for the duration of the noise.

FFT Fast Fourier Transformation

HWA Hot Wire Anemometry

IGV Inlet Guide Vane

Stator blades that reproduce the real high by pass ratio engine first stator. This component is used to set the inlet Mach number and flow angle radial distributions similar to those generated by the engine fan.

NO_x Nitrogen Oxides

OHR Over Heat Ratio

It is the ratio between wire hot resistance, when the wire is electrically heated, and wire cold resistance at ambient temperature.

PSD Power spectral density

Measures the frequency content of a stochastic process and helps to identify periodicities.

RMS Root Mean Squared

SO_x Sulphur Oxides

STT Shielded Thermocouple type T

TRU Temperature Reference Unit

Electronic unit that use Peltier effect to keep one of the thermocouple junction to fix temperature of 0°C

UHC Unburned Hydrocarbons

VKI von Karman Institute

Chapter 1

Introduction

The aim of the present work is to characterize the behavior of an Air Cooled Oil Cooler (ACOC) integrated surface heat exchanger located at the inner shroud of the secondary duct of a high-bypass ratio turbofan. In this chapter the framework of this investigation is presented as well as the test facility and experimental procedure. Starting from the previous studies, the actual situation will be described, underlining the design choices and the physics behind them.

1.1 Introduction

Jet propulsion is a practical application of Sir Isaac Newton's third law of motion *for every force acting on a body there is an opposite and equal reaction*. For aircraft propulsion, the *body* is the air that is caused to accelerate as it passes through the engine. The force required to give this acceleration has an equal effect in the opposite direction acting on the apparatus producing the acceleration.

This section is based on the *The Jet Engine* book, [11], and professor Paganucci *Aircraft Engines Course Notes*, [13]. A turbojet engine produces thrust in a similar way to the engine/propeller combination (turbofan and turboprop engines). Both propel the aircraft by thrusting a large weight of air backwards, one in the form of a large air slipstream at comparatively low speed and the other in the form of a jet of gas at very high speed.

It can be shown that the thrust, T, has the general expression in eq.1.1:

$$T = \dot{m}_e v_e - \dot{m} v + A_e \left(p_e - p_i\right) \tag{1.1}$$

where:

$\dot{m}$ = inlet mass flow rate,
$\dot{m}_e$ = outlet mass flow rate with velocity v_e,
v = upstream asymptotic air speed,
v_e = effective jet velocity,
A_e = exit area,
p_e = outlet pressure,
p_i = inlet pressure.

The last expression states that to increase the thrust the jet velocity should be increased as much as possible, but it's also possible to demonstrate that the fluid kinetic energy[1], KE, is proportional to v_e^2, eq.1.2. When an engine has reached a steady running condition, the energy input to the engine from fuel is almost exactly equal to the extra kinetic energy output (relative to the engine) and the extra jet thermal energy output in some defined proportion. This means that also the fuel consumption is proportional to v_e^2, see also references [11] and [12].

$$KE = \frac{1}{2}\dot{m}_e v_e^2 \tag{1.2}$$

In order to combine these two informations the parameter η_T, thrust efficiency, is introduced. The latter is defined as the useful thrust power over the total mechanical power, eq.1.3, and for a turbojet or a turbofan[2] it assumes the latest form in eq.1.3, giving the behavior in fig.1.1.

$$\eta_T = \frac{P_T}{P_{\text{mec}}} \cong \frac{2v}{v + v_e} \tag{1.3}$$

The thrust efficiency decreases while the ratio v_e/v increases, high efficiencies will be reached with upstream asymptotic air speed as close as

[1]The energy are per unit time, the efficiencies indeed are in terms of powers.
[2]The pressure term in the thrust has not been considered in the expression of thrust and so in the useful power for simplicity.

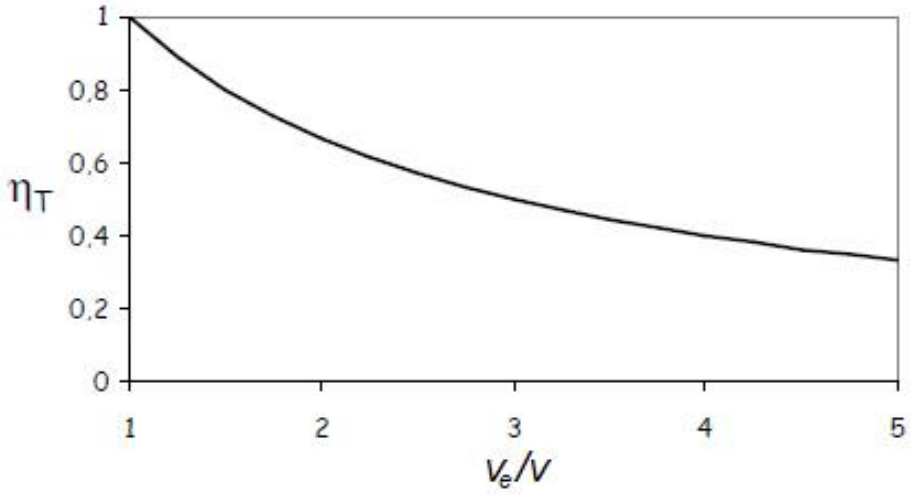

Figure 1.1: Thrust efficiency versus $\frac{v_e}{v}$.

possible to effective jet velocity, see also reference [13].

The high-bypass ratio turbofan permits to have smaller v_e/v respect to turbojet and at the same time to reach the common civil aircraft speeds. This is the main reason for which the turbofan engine are preferred to turbojet for civil transport, see also fig.1.2.

Indeed for a given level of combustion chamber technology, that means fixed thermodynamical efficiency η_{th},

$$\eta_{th} = \frac{P_{\text{mec}}}{P_{\text{th}}} \tag{1.4}$$

where P_{th} = total power input, coming from the combustion of fuel, the overall efficiency η_o, defined as total power output over total power input see eq.1.5, increases with η_T, see eq.1.6.

$$\eta_o = \frac{P_T}{P_{\text{th}}} \tag{1.5}$$

$$\eta_o = \eta_T \cdot \eta_{th} \tag{1.6}$$

1.1.1 Environmental Impact

In recent years, two design requirements have received a high priority from customers and engine manufactures alike:

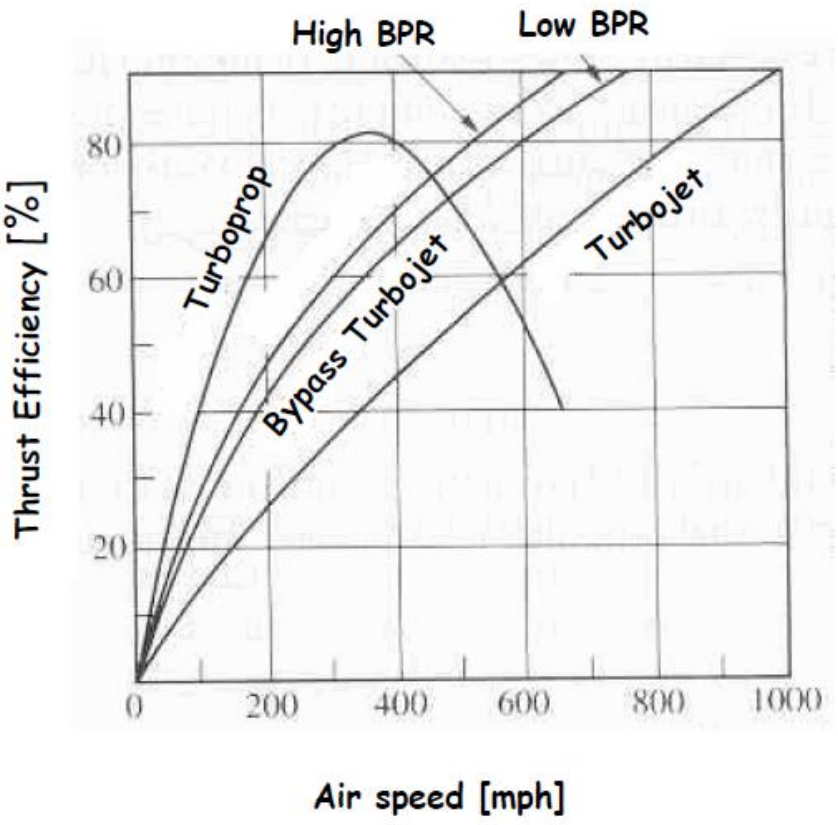

Figure 1.2: Thrust efficiency in function of upstream asymptotic air speed.

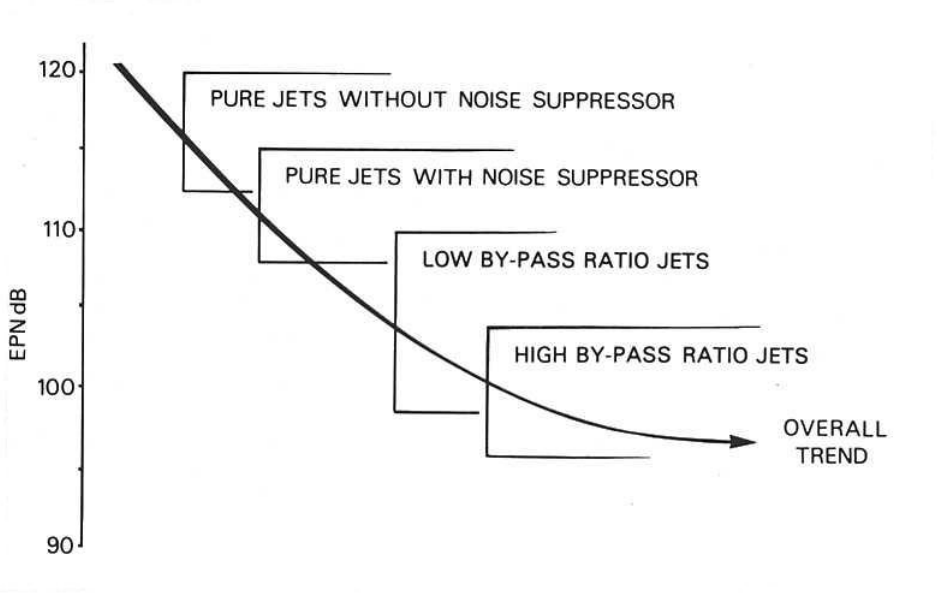

Figure 1.3: Comparative noise levels of various engine types.

- the reduction of noise;
- the reduction of emission.

As shown afterwards the high-bypass engines are the future in order to improve these aspects, so it is important to focus the research on high-bypass ratio turbofans. But, without entering in the depth of the problem, it is also important to understand why a turbofan engine is better regarding noise and pollution emissions.

Noise

To understand the problem of engine noise suppression, it is necessary to have a working knowledge of the noise sources and their relative importance.

The significant sources originate in the fan or compressor, the turbine and the exhaust jet or jets. These noise sources obey different laws and mechanisms of generation (shock waves, mixing flows, turbulence, shearing forces and others sources), but all increase, to a varying degree, with greater relative airflow velocity. Exhaust jet noise varies by a larger factor than the compressor or turbine noise, therefore a reduction in exhaust jet velocity has a stronger influence than an equivalent reduction in compressor and turbine

blade speeds.

With the pure jet engine the exhaust jet noise is of such a high level that the turbine and compressor noise is insignificant at almost all operating conditions. With the bypass principle, the exhaust jet noise drops as the velocity of the exhaust is reduced but the low pressure compressor and turbine noise increases due to the greater internal power handling. The introduction of a single stage low pressure compressor (fan) significantly reduces the compressor noise because the overall turbulence and interaction levels are diminished.

So it is easily understandable how the high-bypass ratio engines have relative low noise emission, see fig.1.3[3].

Pollution

Regarding pollution it is not possible to tell that high-bypass ratio reduces the emission quantity at all, because the combustion chamber (where the pollutants are produced, NO_x, SO_x, CO, CO_2 and UHC) shape and efficiency are almost independent on engine configuration. But the higher efficiency of this type of propulsion system allows to decrease the specific fuel consumption and so the total emissions, given the same combustion chamber efficiency.

1.1.2 Performance

Now is clear the importance of high-bypass concept for the future applications. So the global performances are analyzed to understand how to improve the global efficiency, specifying the relation with ACOC concept.

Writing the thrust equation, eq.1.1, for a turbofan engine it is possible to obtain the eq.1.7, where the subscript f is referred to the fan flow and c to the core flow, finally f is the fuel/air mass flow rate ratio[4].

$$T = \dot{m}_f\,(v_{ef} - v) + \dot{m}_c\,[v_{ec}\,(1+f) - v] + A_{ef}\,(p_{ef} - p_i) + A_{ec}\,(p_{ec} - p_i) \quad (1.7)$$

The previous equation, 1.7, gives us the nominal performances without

[3]The unit that is commonly used to express noise annoyance is the Effective Perceived Noise decibel (EPNdB).

[4]Note that the Bypass Ratio (BPR) is given by $BPR = \dot{m}_f/\dot{m}_c$.

considering some of the main source of efficiency losses. One of the most important is the need of cooling (nozzle cooling, turbine cooling and others). Different methods are used, but they usually require air bleed. Given the inlet flow rate, two are the principal consequences for a turbofan:

- reduction of the outgoing $\dot{m}_f$, if we bleed air from the secondary flow;
- reduction of the outgoing $\dot{m}_c$, if we bleed air from the main flow.

Both the effects reduce the thrust and the overhaul efficiency. The ACOC concept permits to avoid the bleed, or at least to reduce it. However the heat exchanger introduces disturbances on the fan flow to diminishing inefficient nozzle expansion. For this reason the fins under evaluation are oriented almost with the flow direction, fig.1.4.

Theoretically the secondary flow is energized through the heat exchanger, but the entity of this exchange is negligible respect to the pressure losses caused by the fins.

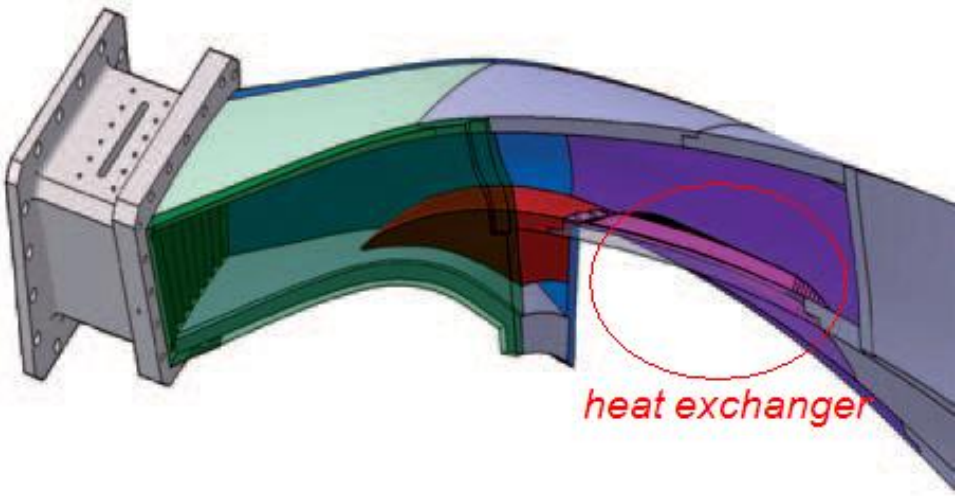

Figure 1.4: Position of the heat exchanger and direction of the fins.

The aim of this project is not only to characterize the actual aerodynamic efficiency of the heat exchanger with the chosen geometry and position, but also to verify the level of the turbulence introduced in the downstream flow and the local flow disturbances caused by the tested configurations.

1.2 Experimental setup

Aerodynamic testing for turbomachinery applications is often carried out in continuous running wind tunnels, which require large power consumption by the compressors.

With the development of high-frequency sensors, intermittent[5] wind tunnels became an alternative to long testing operation.

The experimental work was carried out in a blow-down wind tunnel specifically designed for this application. The design of this facility was driven by the interest on reproducing as close as possible the flow conditions on the region of the separator nose encountered in a real engine, *Villafañe et al.* [3]. The test section allows a proper simulation of the radial and transversal gradients existing in the engine bypass flow, and the reproduction of the radial profiles of Mach number and flow angle along the engine axis. For this purpose the test section walls were designed following engine solid boundaries and flow stream surfaces obtained from Computational Fluid Dynamics (CFD) axisymmetric computations. The flow at the entrance of the test section was reproduced by inlet guided vanes designed using numerical tools.

The wind tunnel provides stable conditions during the test duration.

1.2.1 Wind Tunnel characteristics

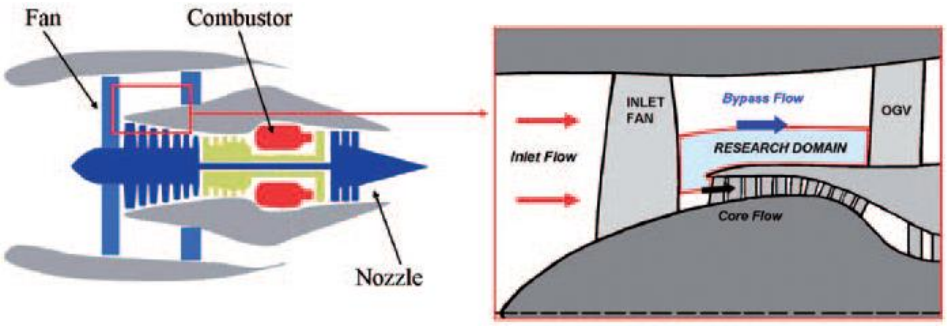

Figure 1.5: Heat exchanger location and research domain.

The wind tunnel is able to reproduce the research domain sketched in fig.1.5 with the following characteristics, (it is possible to find a more detailed

[5]The expression *intermittent wind tunnel* means a wind tunnel in which energy is stored, as compressed air, and then released suddenly to force a large quantity of air through the small throat for a limited period of time, until the tank is empty. The test gas is then released into the atmosphere.

explanation of design choices and computational results in [3]):

- the three dimensional flow characteristics are reproduced;
- in each wall an extra boundary layer is created. Their effects have been accounted for during the test section design, and the flow distributions measured close to those regions are not considered representative for the heat exchanger flow effects evaluation;
- the total temperature is dictated by the expansion on the deposit and the duct circuit guiding the compressed air to the facility, but that is not a control parameter[6];
- the maximum mass flow rate is 6 kg/s;
- the inlet test section area[7] is an annular section of 15 deg with an area of 0.021 m^2.

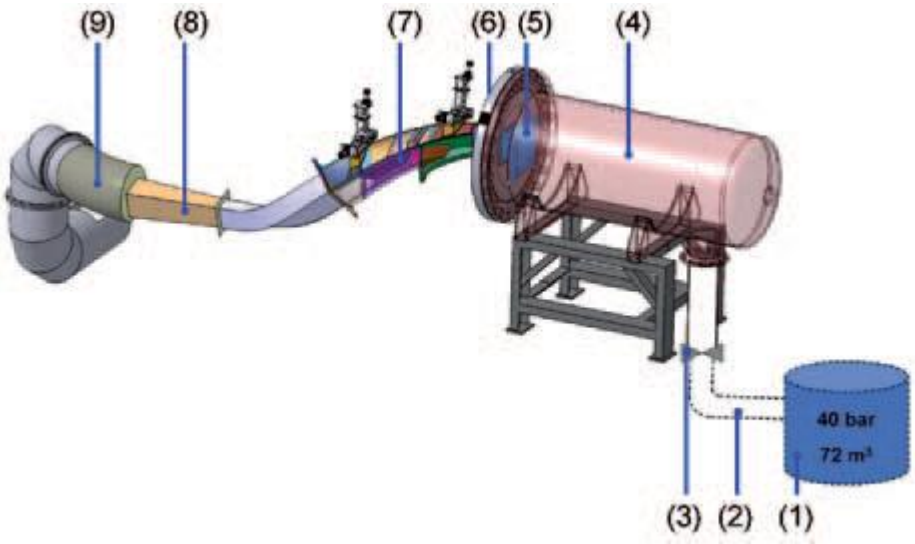

Figure 1.6: Wind tunnel sketch.

A simplified representation of the wind tunnel is shown in fig.1.6, where:

[6]Actually the stagnation temperature does not change during a cruise flight so the results was non-dimensionalized in order to compare the flow, that has different stagnation temperature, during its temporal evolution.

[7]The transversal area of the test section is a compromise between test duration (around 5 minutes) and the convenience of big areas to reduce the influence of wall and instrumentation blockage effects.

1. **40-bar deposit** of 72m^3. It is the air source;
2. **duct circuit** linking the deposit with the settling chamber;
3. **pressure control valve**. This element is operated to keep the Mach number in the test section constant. During the deposit expansion the valve is opened keeping the test section inlet total pressure, that is monitored, constant;
4. **settling chamber**. It is provided with honeycombs and screens that control the turbulence intensity in this element;
5. **inlet contraction**, which accelerates the flow into the test section increasing the uniformity of the flow itself and decreasing the turbulence in longitudinal direction;
6. **Inlet Guide Vane (IGV)s**, they turn and accelerate again the flow to reproduce the radial distributions of Mach number and flow angle downstream of the engine fan;
7. **3D test section**;
8. **diffuser**, in which the core flow is expanded to reduce its velocity before the expulsion[8];
9. **discharge circuit** to the atmosphere.

1.2.2 Measurement planes

Taking into account the research domain of our experiment, see fig.1.5, it was decided to analyze five locations. The first, *Plane 0*, is the reference plane that gives inlet conditions in terms of total temperature, total pressure and inlet turbulence, indeed is located upstream the IGV[9].

The geometry of the other planes of measure is showed in fig.1.7 where, taking into account also fig.1.5:

[8]The air under the splitter is evacuated through a variable area restriction (not visible in the sketch), allowing the control of the mass flow and hence the pressure distribution around the stagnation nose.

[9]Plane 0 is located two times the IGV chord before the beginning of the IGV leading edges.

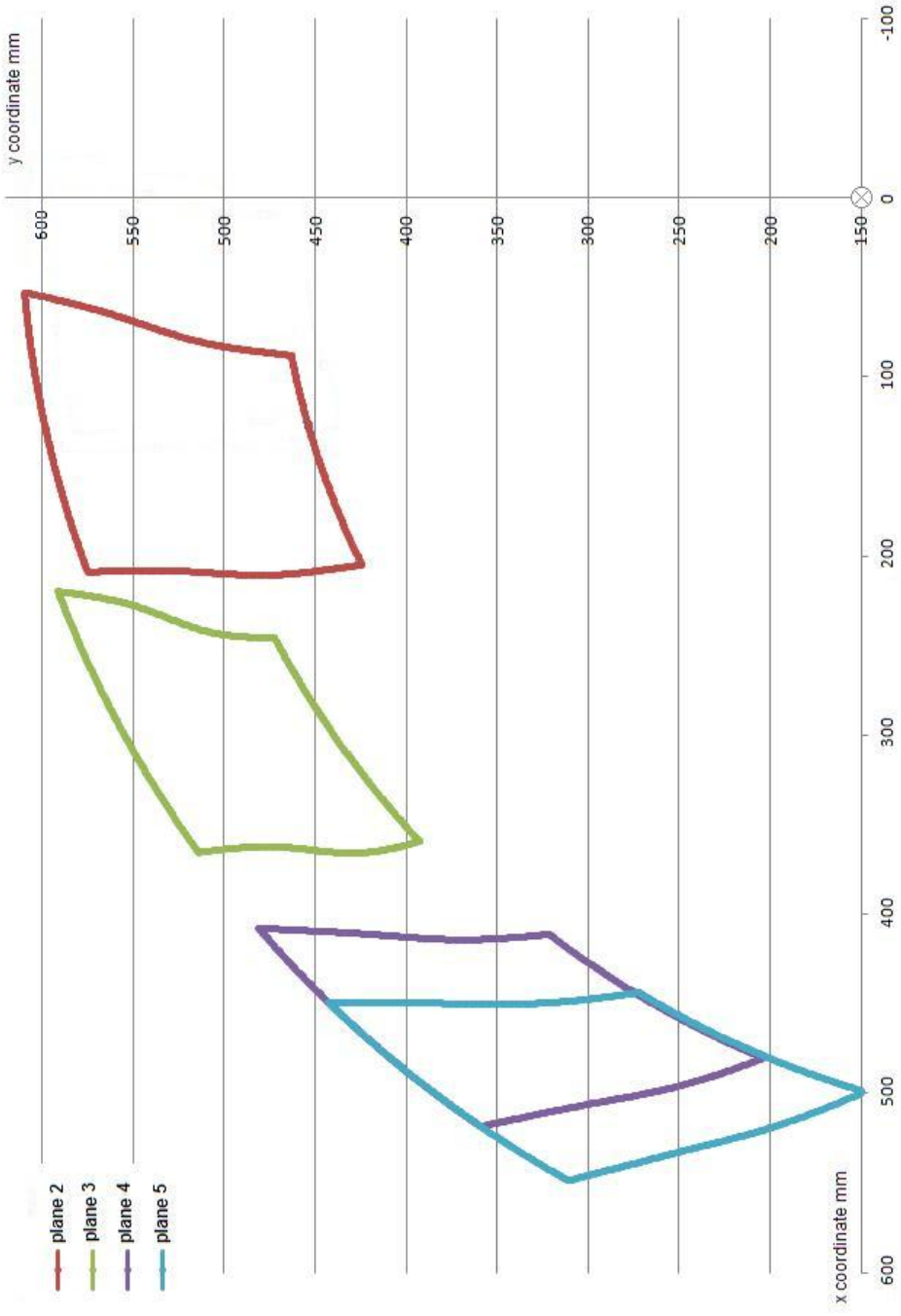

Figure 1.7: Geometry of the five measure planes along wind tunnel.

- Plane 2 is upstream splitter[10];
- Plane 3 is upstream of the ACOC;
- Plane 4 is downstream of the ACOC;
- Plane 5 is before the exit of wind tunnel.

Considering the maximum possible duration of the experiment, the time to move from point to point inside each plane, the time to reach steady value and the acquisition time, different grids were possible but two are the main categories:

- **Coarse grid**: where almost all the plane surface is covered but with less points density;
- **Fine grid**: in which the measure is focused on a restricted region in the central lower part of each plane, the one in which the influence of the ACOC is more important.

Actually sometimes the two grids were combined in an unique intermediate grid, see fig.1.8[11] in which y' is in the direction of immersion and x' is such that $z' \equiv z$.

It is also important to underline the grid common features:

1. the position of one head is linked to the others, it depends on the rake geometry and on the angle of immersion[12] inside the section, see tab.1.1. The angle is evaluated in order to reach most part of the section with the probe;
2. the lower probe head, during its motion, follows a path parallel to the bottom wall[13], but stops itself at each measuring point;

[10]The splitter is the edge where the by-pass flow separates itself from core flow, with the corresponding development of a boundary layer, that is important for the behavior of ACOC, being the latter integrated with splitter surface.

[11]The origin of x', y' and z' reference system is such that the probe is as near as possible to the bottom wall of each section in the position (0,0,0), but with a safe margin that prevents breakages. This security gap is different from probe to probe because the size of each sensor is different, while the origin must be the same. The order of magnitude is a tenth of mm.

[12]The angle of immersion δ is the angle between local vertical and the rake stem, and it is considered positive if in counterclockwise sense, see fig.1.9.

[13]Possible deviations from nominal path are possible because of not perfect synchronization between the two engines that move the rake, one for vertical and the other for horizontal movement.

3. a sufficient safe margin is always present from the bottom wall as well the lateral and upper walls;

Plane	δ **[**deg**]**
0	0
2	5.9
3	4.6
4	−8.8
5	−9.5

Table 1.1: Angle of immersion per each measurement plane.

Finally in each measurement plane three different configurations are analyzed:

1. the *clean* configuration, that is without any heat exchanger;
2. the configuration with the *continuous fins* heat exchanger, see fig.1.11a;
3. and with the *interrupted fins* heat exchanger, see fig.1.11b.

It is worth to note that even the configurations 2 and 3 are analyzed without heating up the fins. Only the aerodynamic effect of the integrated heat exchanger is investigated, not the thermal aspect.

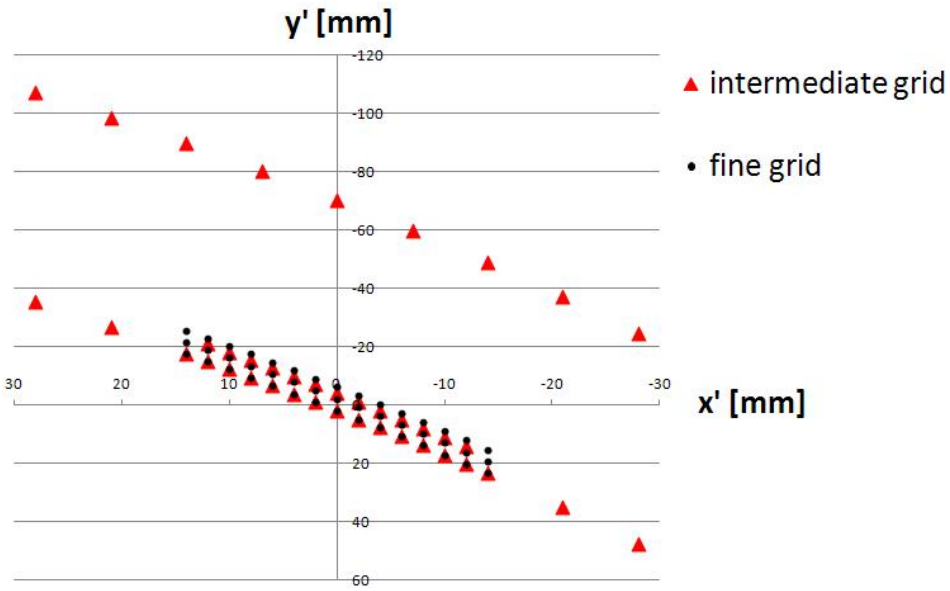

Figure 1.8: Plane 5 measurement grids examples.

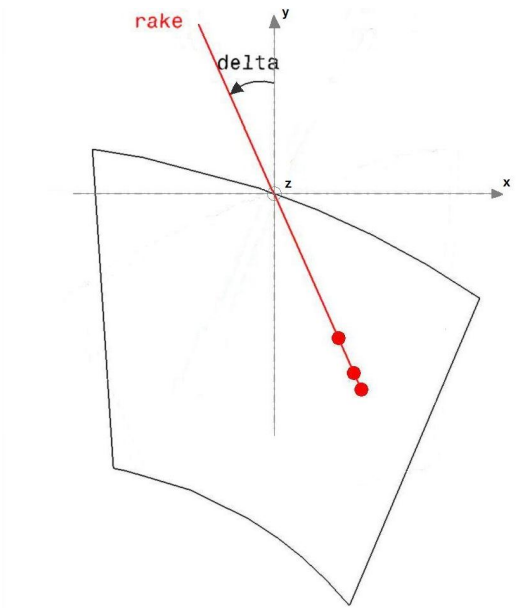

Figure 1.9: Angle of immersion δ of the STT probe rake.

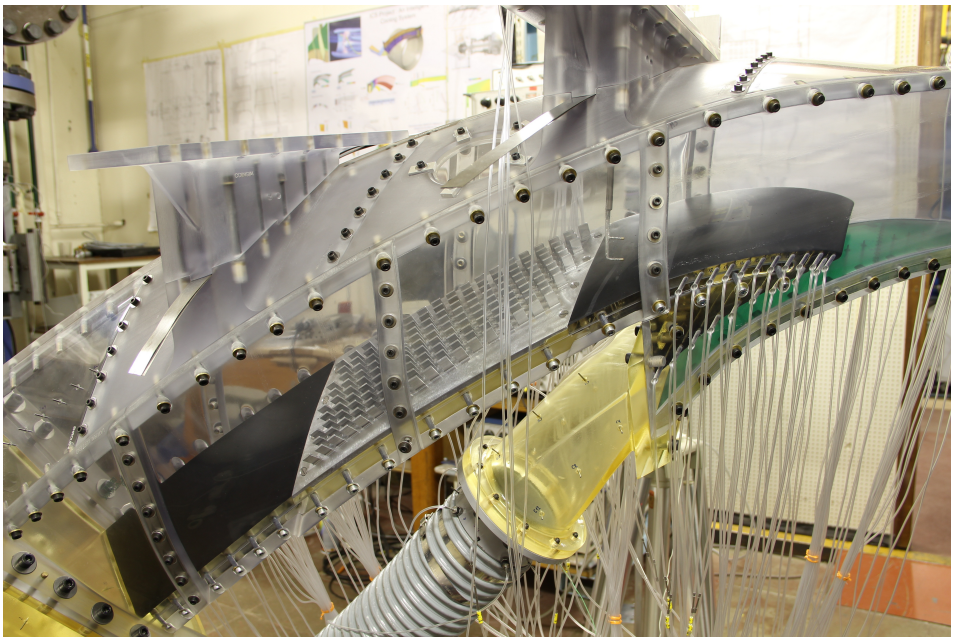

Figure 1.10: Picture of the test section.

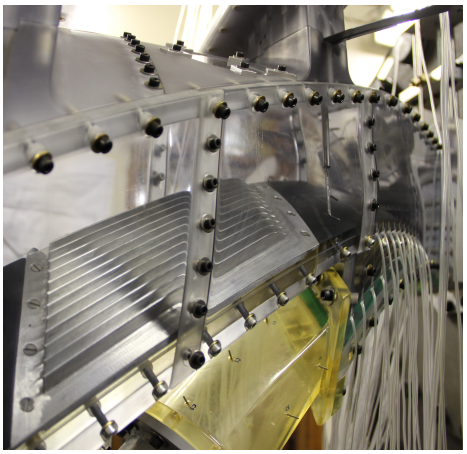

(a) Continuous fins heat exchanger.

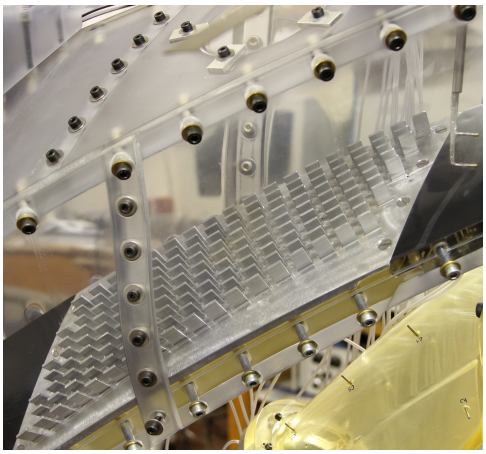

(b) Interrupted fins heat exchanger.

Figure 1.11: Tested heat exchanger configurations.

Part I

Measurement background

Chapter 2

Temperature measurements

Before starting with the measures it is important to introduce the used probes and to describe their functioning. First of all the temperature analysis was done. In this chapter, after the description of the used probes (thermocouples) the measurement chain is investigated and at the end the results of the probe calibration are presented.

2.1 Probe description

Thermocouples for accurate gas temperature measurements require appropriate probe design for a given application and precise characterization of the probe performances. The chosen thermocouples are Shielded Thermocouple type T (STT) with a wire diameter of 25 µm, fig.2.1. Other informations are shown in tab.2.1[1]. A numerical study of the probe static and dynamic characteristics was done by *Villafañe et al.* and can be found in references [2] and [4].

Materials	**Sensitivity**	**Linear range**
copper/constatan	43 µV/°C	-200 to 350 °C

Table 2.1: Type T thermocouple characteristics

[1]The constatan is copper/nickel alloy.

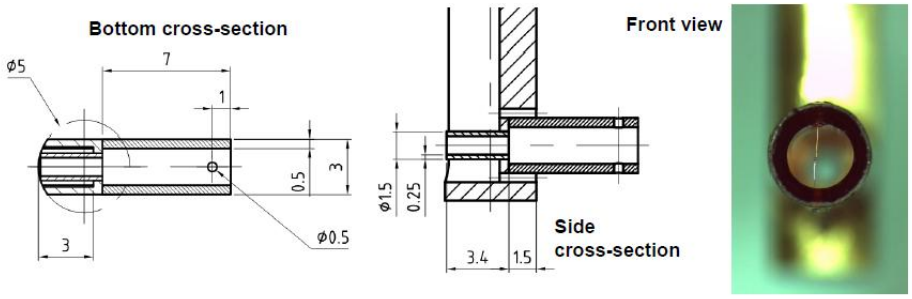

(a) Probe head design.

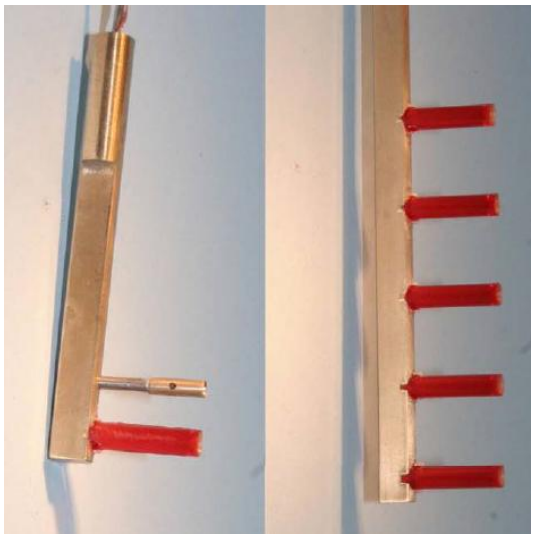

(b) Single and rake probes.

Figure 2.1: Thermocouple examples.

2.2 Measurement chain

Whenever a thermocouple measure is done it is important to investigate the entire measurement chain formed by:

- **extension cables**, used to connect each probe head to the corresponding channels of the Temperature Reference Unit (TRU);
- **TRU**, used to minimize the cold reference junction error, see also [6]. The chosen reference box is *TRU 937 model 100*[2], fig.2.2, which keeps the cold junction to a temperature of $0 \pm 0.03°C$;
- **Amplifier for type T thermocouples**, the thermocouples signal is in the order of mV and the amplifier has a gain around 2500. This amplifier is VKI made and has a low pass filter at 10 kHz;
- **Data Acquisition System (DAS)** and **acquisition software**[3].

Comparing the signals recorded during the calibration and the tests, the analysis of the noise level allows to discern the frequency content disturbances resulting from the operational condition and from the measurement chain.

Finally the interpolation was done with Root Mean Squared (RMS) method, using the MATLAB command *polyfit*.

Figure 2.2: Temperature reference unit.

[2]For more details see `http://www.isotech.co.uk`.

[3]Labview is the chosen software. During the calibration a sample frequency of 1 kHz was employed

2.3 Calibration

It is necessary to characterize the behavior of each thermocouple head. The possible calibration ways are principally three:

1. calibration using physical invariant points;
2. oil bath calibration;
3. oven calibration.

The first is the most precise calibration but requires the necessity to keep the used substance at its triple or double points, moreover the probe should be in contact with the selected gist and, depending on the material, this is a strong constriction because of the difficulty to clean the thermocouple after the calibration, must not forget the extremely small dimension of the probe. Also for the oil bath the same problem shows. Hence finally the oven calibration was chosen.

2.3.1 Oven calibration details

To know the oven temperature during the calibration other bare type K thermocouples were used[4]. The type K ones were posed in front of each type T probe head[5] to avoid possible sources of inhomogeneity due to temperature stratification inside the oven, and the complete set of bare and shielded thermocouples was enclosed in a cylindrical conductive material, copper, to minimize convection error caused by internal flows due to the presence of an oven fan, see fig.2.3.

The resulting voltage/temperature characteristic lines are summarized in tab.2.2. Probe 1,2,4 and 5 are the rake heads, used to measure from plane one to four, while 0,6 and 7 are the single head probes that were placed in plane 0 of the helical wind tunnel to have the total inlet temperature time evolution. The probe 3 results are not present here since they were found to be defective.

[4]These ones were calibrated in an oil bath previously using an alcohol thermometer posed near to the thermocouples junctions to minimize convection errors inside the bath.

[5]Three single probes and a rake with 4 working heads had to be calibrated.

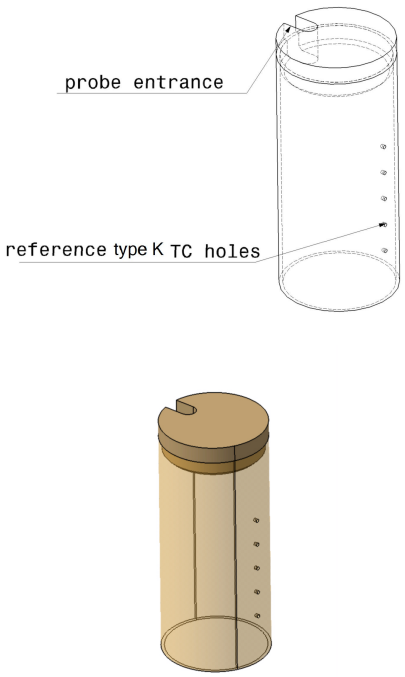

Figure 2.3: Envelope used in the oven calibration.

2.3.2 Noise tests

Before the actual tests is important to characterize the level and the type of noise to distinguish it from the one resulting from the measurement. Each element of acquisition chain introduces some disturbances in the output signal, comparing different possible combination the following results are achieved:

- each amplifier channels have different gain, see tab.2.3, and different

	Slope (°C/V)	Offset (V)	Correlation coefficient (R^2)
STT0	9.7361	1.1436	0.999990
STT1	9.8188	1.0353	0.999928
STT2	9.7054	1.1008	0.999978
STT4	9.7397	1.2747	0.999991
STT5	9.6861	2.0258	0.999964
STT6	9.6786	0.1929	0.999923
STT7	9.7428	-0.2618	0.999945

Table 2.2: Characteristic slope and offset of used STT

Chs Number	Gain
1	2423
2	2417
3	2225
4	2474
5	2335
6	2529
7	2624
8	2650
9	2266
10	2435
11	2483
12	2596

Table 2.3: Gain of each type T amplifier channels

noise level, see tab.2.4;

- channels 4,7 and 11 have the lowest noise, see tab.2.4, hence these are employed in measurement each time is possible;
- grounding the channels to earth or to some common box is useless from the point of view of reducing signal disturbances;
- changing extension wire, TRU channels or DAS channels does not vary anything in the output.

Amplifier channel	**Average**	**Standard (or RMS) deviation**	**Coefficient of Variation (CV)**
1	2.235 V	$20.5 \cdot 10^{-3}$ V	$9.2 \cdot 10^{-3}$
2	2.230 V	$20.9 \cdot 10^{-3}$ V	$9.4 \cdot 10^{-3}$
3	2.053 V	$24.2 \cdot 10^{-3}$ V	$11.8 \cdot 10^{-3}$
4	2.181 V	$7.0 \cdot 10^{-3}$ V	$3.2 \cdot 10^{-3}$
5	2.154 V	$19.6 \cdot 10^{-3}$ V	$9.1 \cdot 10^{-3}$
6	2.333 V	$25.3 \cdot 10^{-3}$ V	$10.8 \cdot 10^{-3}$
7	2.420 V	$9.4 \cdot 10^{-3}$ V	$3.9 \cdot 10^{-3}$
8	2.444 V	$34.1 \cdot 10^{-3}$ V	$14.0 \cdot 10^{-3}$
9	2.091 V	$23.9 \cdot 10^{-3}$ V	$11.4 \cdot 10^{-3}$
10	2.246 V	$38.8 \cdot 10^{-3}$ V	$17.3 \cdot 10^{-3}$
11	2.291 V	$9.5 \cdot 10^{-3}$ V	$4.1 \cdot 10^{-3}$
12	2.395 V	$40.1 \cdot 10^{-3}$ V	$16.7 \cdot 10^{-3}$

Table 2.4: Noise of each channel at T_{amb} without filtering.

It was investigated also the frequency composition of the different signals doing the *Fourier Transformation*, using the Fast Fourier Transformation (FFT) algorithm developed by *Coole and Tukey*, see also [9]. An electronic noise each 50 Hz is recognized, see fig.2.4 and 2.5; this type of noise is due to the alternate current 50 Hz frequency that feeds each electronic device, even if the alternate current is transformed to continuous current[6]. It is clearly visible also the different level of noise present in different amplifier channels comparing the two aforementioned figures.

2.4 Buffer memory test

A preliminary test on the DAS was done to know the actual number of samples that could be stored inside the DAS memory[7] and it was found that the maximum is 10^7. So knowing the duration of experiment the maximum sampling frequency is deduced, depending on number of connected channels.

[6]The transformation is not ideal, the result of this process is a continuous current but with a noise at 50 Hz (and its multiples) frequency.

[7]All the data are collected firstly in buffer memory and then transferred to computer at the end of measure.

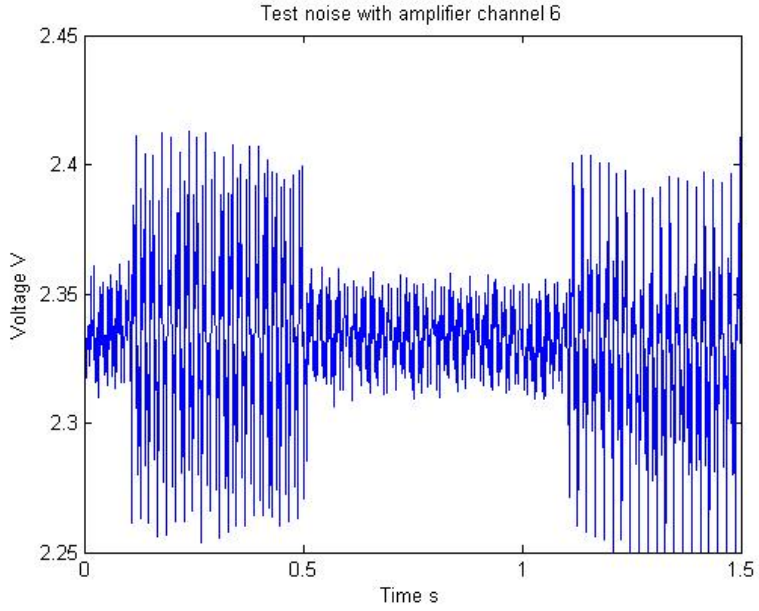

(a) Signal shape.

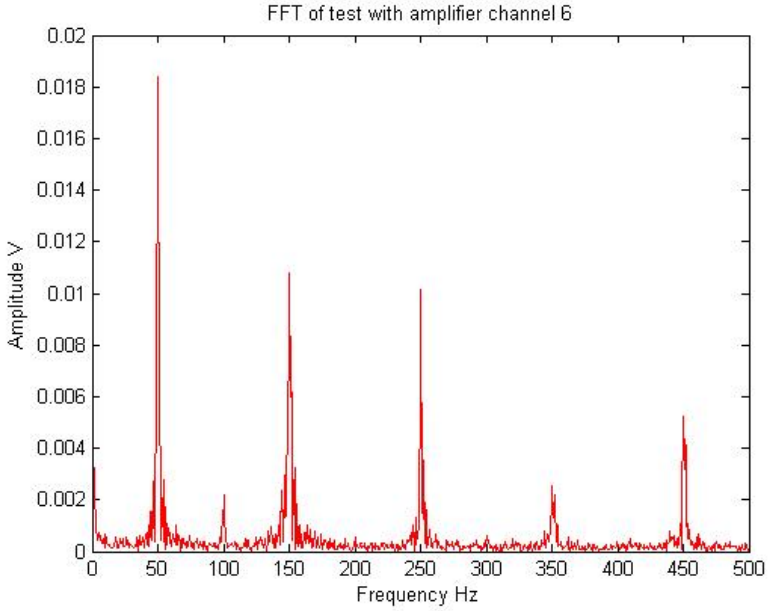

(b) Fourier transformation.

Figure 2.4: Signal deriving from amplifier channel 6.

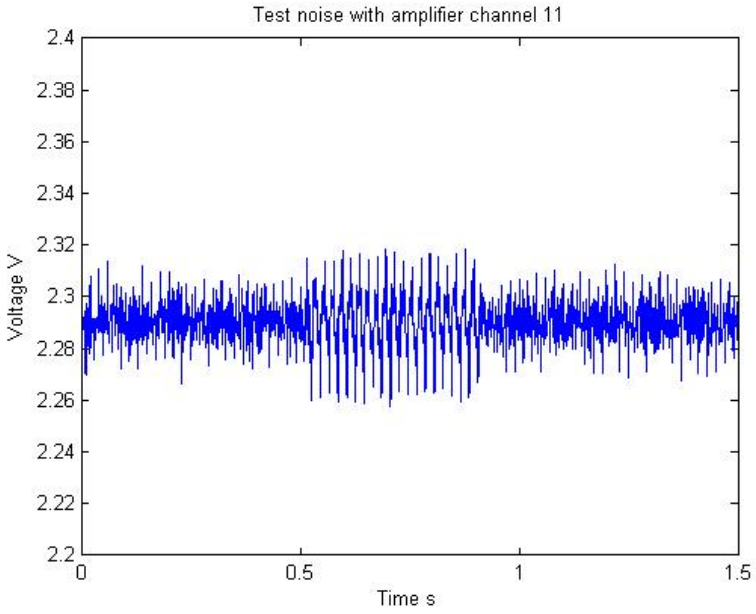

(a) Signal shape.

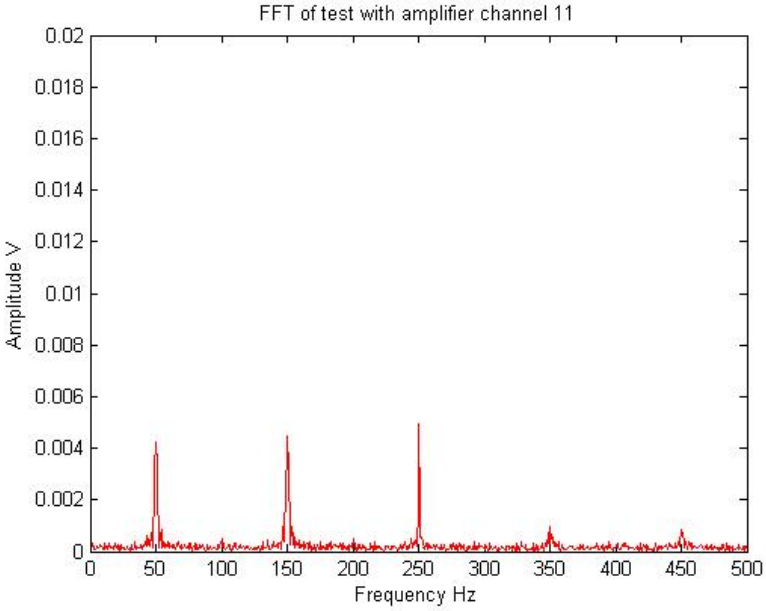

(b) Fourier transformation.

Figure 2.5: Signal deriving from amplifier channel 11.

Chapter 3

Pressure measurements

The pressure measurements are part of the ACOC project, but are not treated in this work. The chapter gives a list of the these measures.

To be exhaustive in the description of the pressure devices an entire report is needed. So in this work several aspects were not taken into account, but the results are used.

3.1 Total pressure measurement

In each plane of measurement a total pressure map is available for different heat exchanger configurations.

The adopted probe is a six heads rake, fig.3.2, and each sensing element is a Pitot tube. The pressure signal is converted in analog signal by a scanner[1], fig.3.1.

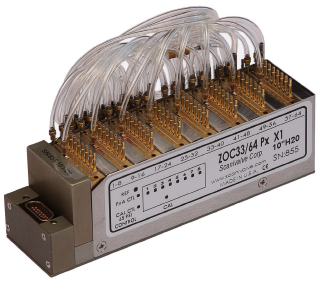

Figure 3.1: Pressure scanner.

[1]To have further informations see `http://www.scanivalve.com/`.

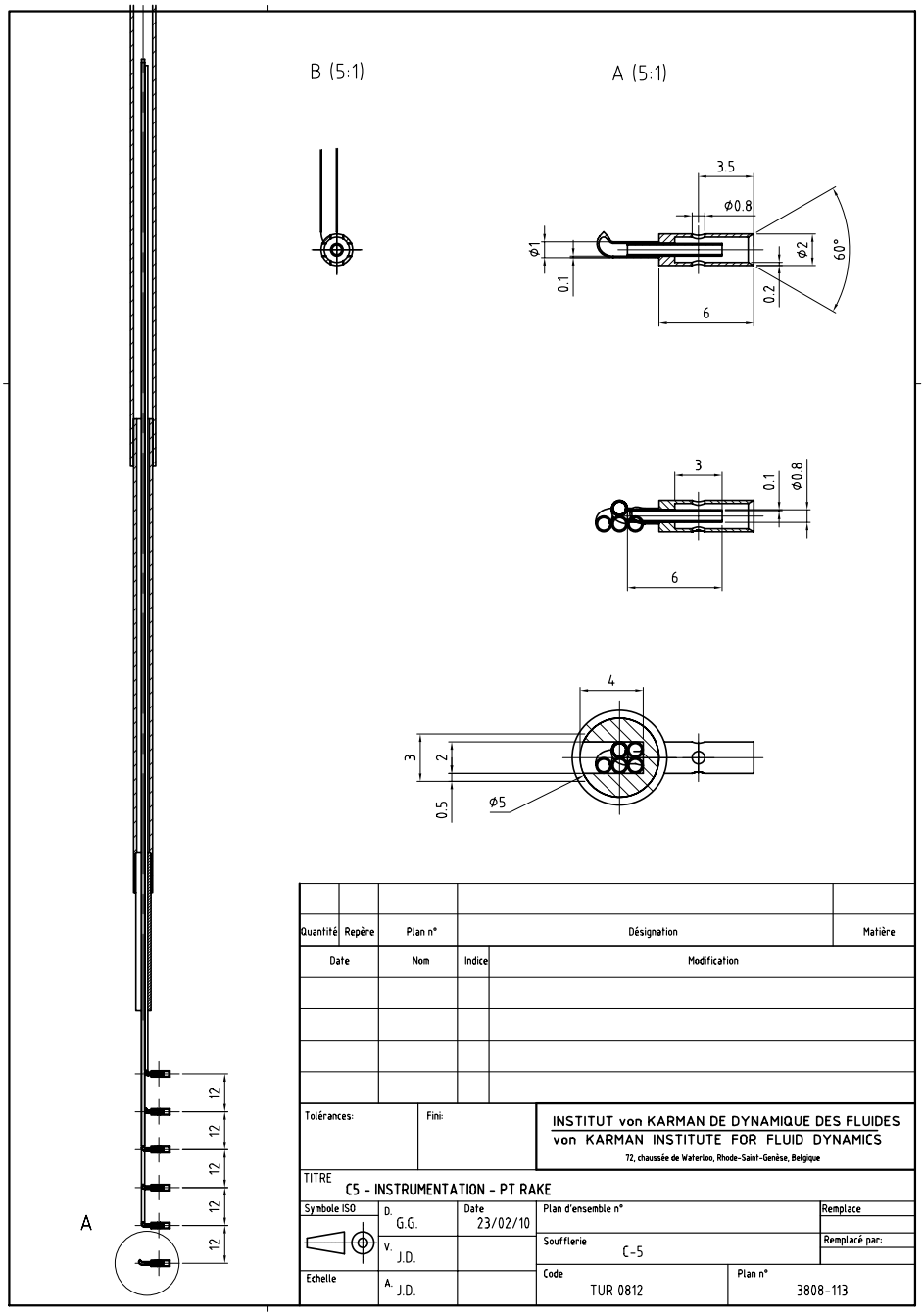

Figure 3.2: Pitot tubes rake sketch.

3.2 Static pressure measurement

The same scanner used for the total pressure is used also for static pressure. The difference here is that instead of a Pitot several static pressure taps are all along the facility middle line and also in the bottom wall of each measurement plane, fig.3.3.

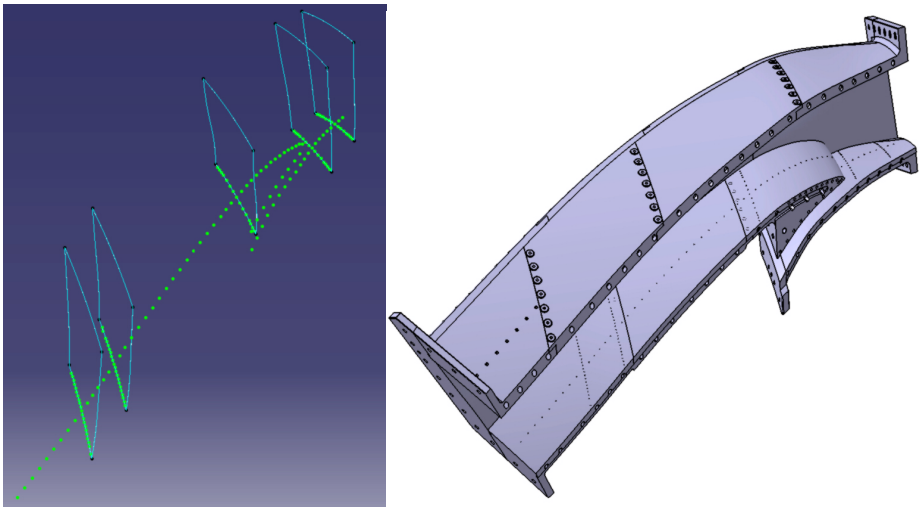

(a) (b)

Figure 3.3: Static pressure taps position.

3.3 Five holes probe

The last type of pressure probe is the five holes one. The rake has two heads, as shown in the fig.3.4.

This probe uses the difference in the measured pressure between hole and hole to reconstruct the flow angle respect to the probe direction. That device was also employed to measure the static pressure inside a measurement plane section.

The calibration of this type of probe is not trivial and requires some numerical post processing to can be used. In the following the flow angle data coming from this measurement was employed to correct the hot wire data whenever this probe was used to measure the flow velocity.

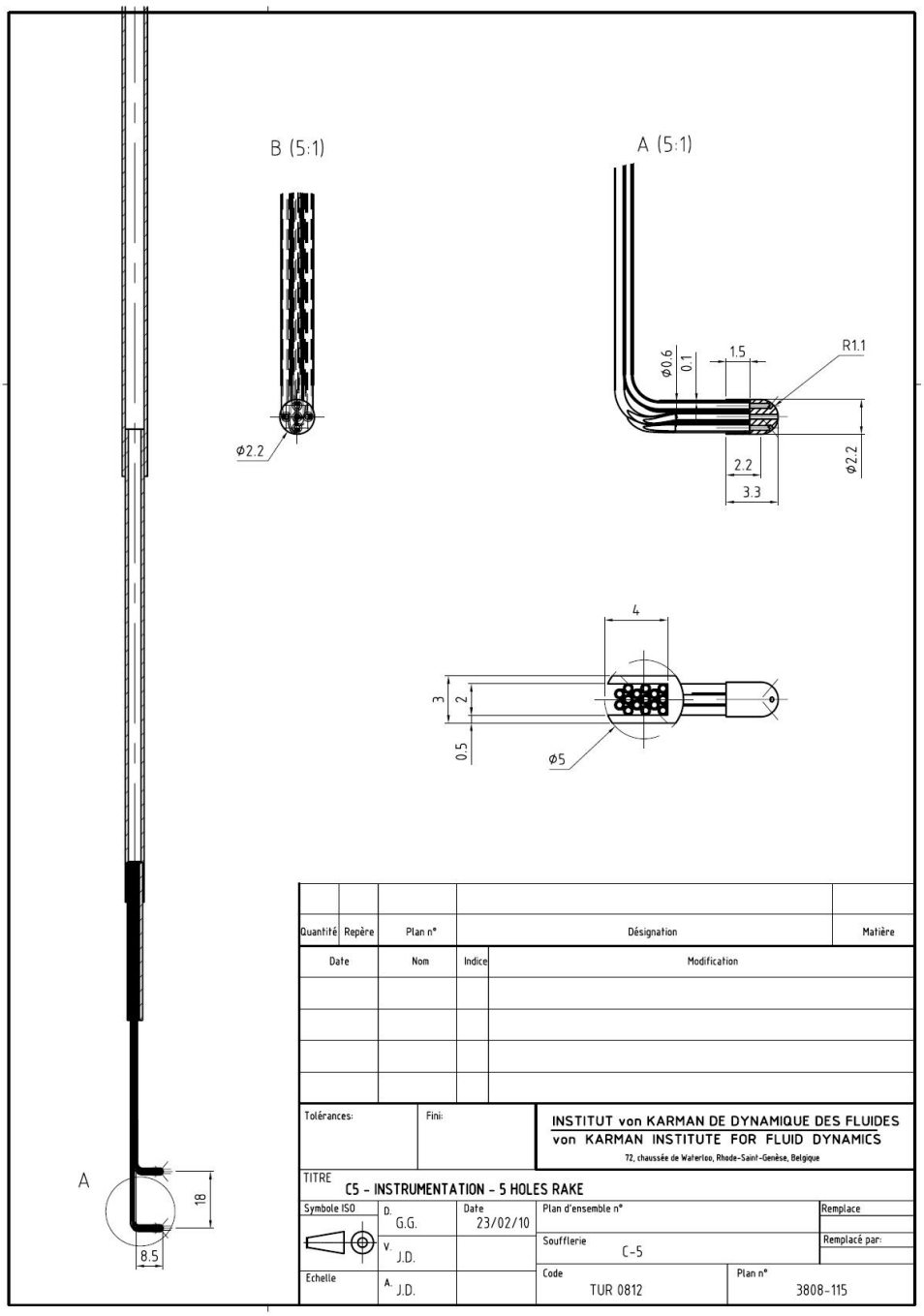

Figure 3.4: Five holes rake sketch.

Chapter 4

Hot Wire Anemometry measurements

The last important measurement technique used during the test campaign is the Hot Wire Anemometry (HWA). This device allows the evaluation of the high frequency velocity fluctuations. The most used instrument for these type of measures is the *Hot Wire Anemometer*, because of its fast response capability, possibility of high spatial resolution (also inside the boundary layer), and eventually low blockage effects[1].

Mean velocity mapping, flow angle determination and turbulence intensity are the typical quantities that this technique measures. In particular this work is focused on the turbulence evaluation, that plays a role in the generation of fluid friction losses and so in the quantification of the aerodynamic efficiency of the heat exchanger. High frequency velocity fluctuations have to be estimated both into the core flow both inside the boundary layer.

After a small working explanation of the used technique, the results of calibration and the procedure employed are shown and explained in this chapter.

4.1 Introduction

The HWA is a thermal anemometry technique based on heat transfer from heated thin wires by relating the thermal convection to the consumed electrical power. This heat transfer, for a given probe/fluid combination, can be

[1]The hot wire probe can be arranged in very slender configuration.

related to instantaneous flow velocity, density and total temperature. High frequency resolution[2], up to 1 MHz for thin wires in high speed flow, could be reached.

The principal techniques are divided in:

- Constant Current Anemometry (CCA), widely employed in the past because it does not require fast feedback and control loop;
- Constant Temperature Anemometry (CTA);
- Constant Voltage Anemometry (CVA), not sufficiently mature.

As the name indicates the main difference consists in maintaining the probe at constant current, temperature and voltage respectively, but the CTA has some advantages for the present application as:

1. it is already available and completely validated[3];
2. smaller wire temperature fluctuations[4] respect to CCA;
3. higher frequencies response reachable respect to CCA.

So finally is the selected one.

4.2 Constant Temperature Anemometry

The book *Measurement techniques in fluid dynamics* [1] is adopted in the following pages as the reference for the functioning explanation of the Constant Temperature Anemometry (CTA).

The hot wire anemometer consists of a sensor, a small electrically heated wire exposed to the fluid flow, and of an electronic equipment, which performs the transformation of the sensor output into an useful electric signal, but in the case of this type of measurement the electronic circuitry is an integral part of the anemometric system and has a direct influence on the probe characteristic.

[2]The frequency limitation is given mainly by the thermal inertia of the wire and, for techniques that imply a closed loop control (as the one used in this work), by the control system response velocity.

[3]The CVA is still research argument.

[4]Theoretically if it would be possible to keep strictly constant the wire temperature the only output voltage variation should be flow related.

The purpose of the constant temperature electronic circuit is to give to the wire a controlled amount of electrical current in order to maintain the wire temperature constant when the amount of heat transfer varies. In this way only the flow is the responsible of the heat exchange variation.

A typical configuration for this type of measurement is shown in fig.4.1, but it is worth to note how the control circuit works.

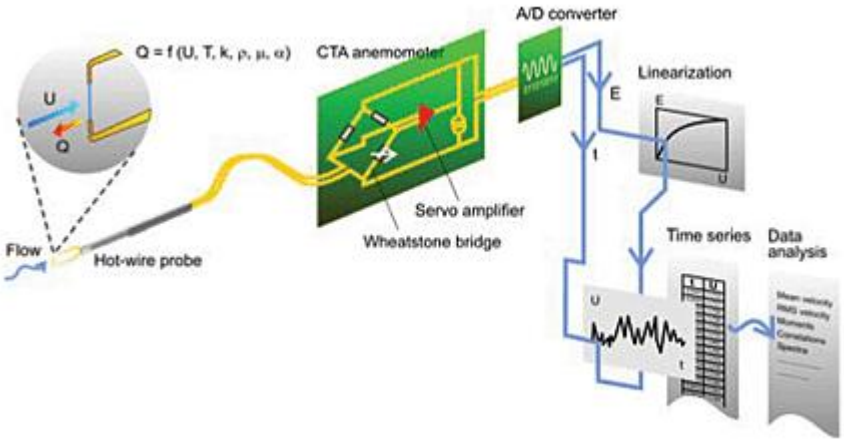

Figure 4.1: Typical anemometric system.

Using as reference the fig.4.2 it is possible to understand the CTA control circuit principle. Briefly, the Wheatstone bridge error voltage, e, is amplified and used to control the current supply, $C.S.$, in order to modify the supply voltage and so to keep the wire temperature constant. The temperature value is set by adjusting the bridge resistance, R.

The CTA technique limits the wire temperature changes respect to CCA, implying a minor role of the wire thermal inertia. However to evaluate the maximum cutoff frequency of the entire system, that limits the maximum frequency detectable of the physical flow phenomena, it is necessary to consider the still simplified circuit of fig.4.3, that leads to a resonance frequency

$$\omega \;=\; f\big(\frac{R_w}{R_0}, H, E, M_1, M, K, L\big) \tag{4.1}$$

where

R_w = wire hot resistance,
R_0 = wire cold resistance,
H = hot wire correlation equation function of the velocity,
E = output voltage,
M_1 = electronic circuit time constant,
M = wire and cables time constant,
K = amplifier gain,
L = compensation inductance.

The inductance L is used to minimize the effects of M and M_1 in order to obtain a critically damped system, with a frequency response as flat as possible. The answer depends also on the output voltage of the sensor, that varies when the flow velocity changes, this is why the inductance has to be adjusted for the velocity range foreseen. For more details on hot-wire working and optimization see the reference [16].

4.3 Probe

As previously said in the hot wire anemometry the entire measurement chain has an influence on the sensor setting, so each component is analyzed:

- wire
- support
- control module
- acquisition system

The probe used during these experiments is a rake of six single wire heads, see fig.4.4. Each sensing element (wire plus support) is linked with a BNC cable to a control module, and eventually from each control module the signal is acquired with a single data acquisition system.

Wire and Support

The characteristics of the wire is summarized in table 4.1.

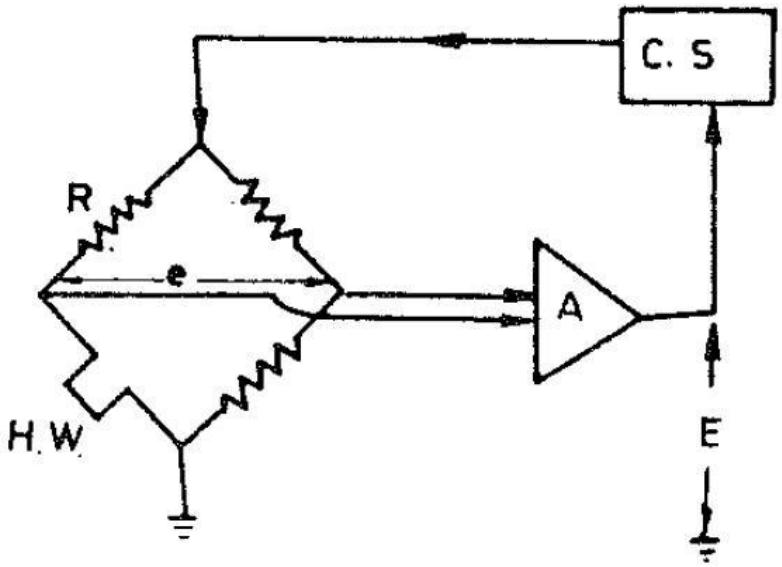

Figure 4.2: Schematic control circuit for CTA.

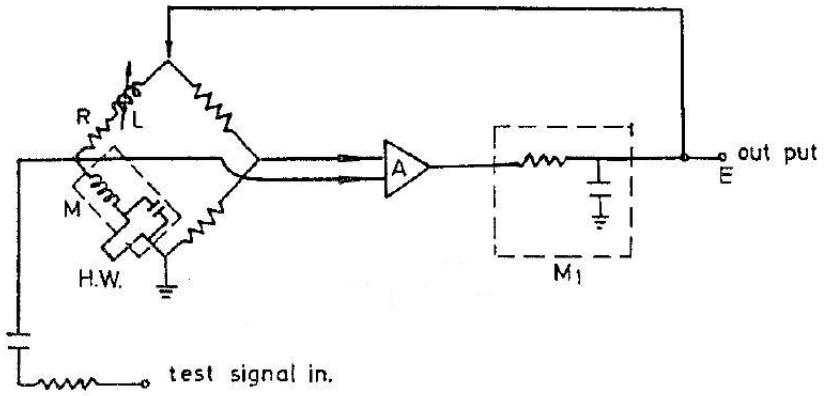

Figure 4.3: Control circuit for CTA, considering the cabling influence.

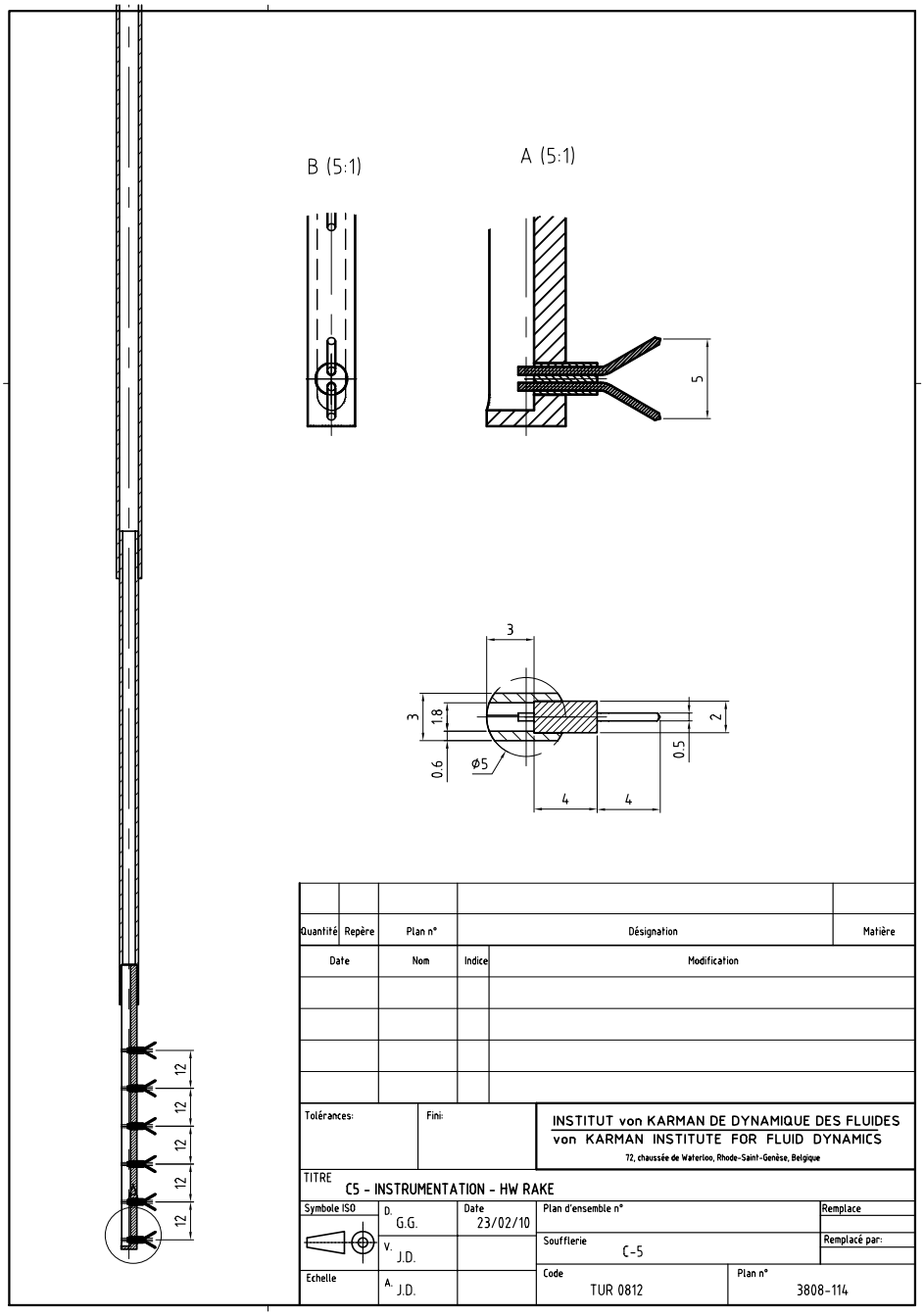

Figure 4.4: Hot-Wire probe drawing.

length	5 mm
diameter	9 µm
active length	1.5 mm
sensor material	tungsten
coating	6.7 % platinum
temperature resistance coefficient	0.00320 1/K

Table 4.1: Sensing wire characteristics.

Another important parameter is the wire resistance because, together with the Over Heat Ratio (OHR), it fixes the wire temperature and so the sensor response velocity (function of the ΔT between wire and flow mean temperature).

Starting from the upper head (number 1) to the bottom head (number 6) in tab.4.2 it is reported the different resistances.

Head number	**resistance [Ω]**
1	1.835
2	1.052
3	1.728
4	1.481
5	1.707
6	1.600

Table 4.2: Wire cold resistances.

The prongs are steel made with a resistance of 0.110 Ω. Knowing the wire resistance and the prongs resistance it is possible to evaluate the support resistance just subtracting them from the total resistance. The results are in tab.4.3.

Support relative to probe number	**resistance [Ω]**
1	1.767
2	1.562
3	1.784
4	1.829
5	1.828
6	1.985

Table 4.3: Support resistances.

Control module

Two different control modules are employed.The three bottom sensors use a *Dantec*[5] technology, and the three upper ones use a VKI made control circuit. The last is a constant over heat ratio circuitry.

1. *VKI* control module, see fig.4.5.

Figure 4.5: VKI made Hot-Wire CTA control circuit.

As previously said the way of working of this circuit is to measure R_0 and to keep constant the OHR, where:

$$\text{OHR} \;=\; \frac{R_w}{R_0} \tag{4.2}$$

but the relation between wire resistances, R_w or R_0, and wire temperatures, T_w or T_0[6], is:

$$R_w \;=\; R_0\left[1+\alpha_0\left(T_w - T_0\right)\right] \tag{4.3}$$

This means wire temperature, T_w, constant only if the initial wire

[5]Dantec is a brand specialized in hot wire anemometry, more informations on the functioning are available in references [18] and [19].

[6]The subscript 0 is referred to wire cold (ambient) condition, while w to wire hot condition.

resistivity, α_0, the initial resistance, R_0, and so the initial temperature, T_0, are constant.

However the initial conditions vary from test to test and T_w is not really constant during the complete test campaign.

Finally the resistance measured from the control circuit is not R_0, but the total wire + support + BNC cable resistance, R_{TOT0}; so what we can control is the ratio $R_{\mathrm{TOT}}/R_{\mathrm{TOT0}}$. Knowing the support and the cable resistance it is possible to evaluate the real OHR, see also appendix A.

Probe number	**Set OHR**	**Real OHR**
1	1.1	1.22
2	1.1	1.30
3	1.1	1.23

Table 4.4: Over Heat Ratios.

2. *Dantec* control module, see fig.4.6.

Figure 4.6: Dantec Hot-Wire CTA control circuit.

It is a true Constant Temperature Anemometry (CTA) circuit. To describe the actual way of working of this complex device is not trivial, but the most important feature that differentiates these modules from the previous ones is the possibility to keep really constant the wire temperature[7], selecting the appropriate option during the calibration.

[7]It is possible also to work in constant over heat ratio mode, but this imply less precision in the output voltage, or at least a dependence of the output on the wire temperature.

Varying from test to test the ambient temperature, and so the wire cold resistance, in order to maintain T_w at the same value it is necessary that the module slightly changes the set OHR each time the wire is switched on. However the initial OHR is 1.57, this value is bigger than the one used for the wires 1, 2 and 3 and it is permitted by the several safe controls present inside the *Dantec* modules. Between them there is a maximum allowed wire temperature check, this is why it is possible to increase T_w without burning the wire.

Finally it is worth to note that it is needed to know the characteristics of the used BNC cables from the probes to the modules. Between the input parameters necessary to allow the *Dantec*[8] software to measure the right resistance and inductance of the circuit there are the BNC cable resistance and impedance. While for the resistance it is not a problem, to measure the inductance (and so the total impedance) is not easy; so unified cables are used, see tab.4.5.

Length	20 m
Resistance	1 Ω
Impedance	50 Ω

Table 4.5: Unified BNC cables details.

Figure 4.7: National Instrument USB-6255.

[8]This software is called *Streamware*.

Acquisition system

Lastly, regarding the acquisition system, the chosen device is the DAS *NI USB-6255*, see also fig.4.7. Indeed this multiplexer has a maximum sampling rate of $750/n$ kHz where n is the number of input channels[9], sufficient for our applications; even for the hot wire one that requires the biggest sampling frequencies in order to mark the turbulence scale.

4.4 Calibration

The possible relations between the output voltage, V, and the velocity, u, are the exponential

$$V = A + Bu^n$$

or the fourth order polynomial,

$$u = a + bV + cV^2 + dV^3 + eV^4$$

but the latter gives a better data fitting[10]. Sometimes it is better to give non-dimensional relation in Reynolds and Nusselt number, that has the following expression:

$$Re = f(Nu)$$

.

A first set of calibration in velocity and voltage was done (using the fourth order relation) and the results are shown in tab.4.6. While a second non-dimensional calibration in Nu and Re was done right after in order to take into account the effects of the possible difference in flow total temperature between the calibration and the tests. The dimensional calibration is more precise because does not imply numerical correction or iteration, as the non-dimensional one, but it is not applicable if there is a significant total temperature variation between calibration and test, but also during a single experiment. Finally the dimensional calibration was chosen.

[9] To have further information see `http://italy.ni.com/`.

[10] Historically the exponential relation was the most used before the diffusion of the modern computers with high computational capabilities that allow the high order polynomial fitting.

Wire	a	b	c	d	e
1	14160.87	-23423.15	14382.14	-3887.34	393.54
2	10012.86	-15560.48	8973.70	-2281.82	218.30
3	17455.27	-28165.63	16869.92	-4448.10	438.80
4	34.63629	25.70276	8.74980	-1.75197	0.23635
5	30.22715	9.61723	4.09269	-0.51748	0.03130
6	31.22490	15.00048	1.56112	-0.06180	0.00529

Table 4.6: Hot Wire probe dimensional calibration.

Probe number	R^2
1	0.99904
2	0.99830
3	0.99953
4	0.99998
5	0.99995
6	0.99995

Table 4.7: Dimensional calibration R^2.

4.4.1 Square wave test

Another important parameter during the calibration is the square wave test. Adjusting the inductance and the resistance of the control circuit it is possible to improve the limiting frequency of the system. The risk is to not have sufficient damping and so to self-maintain the oscillations. The best is to have a critically damped system.

The answer of a second order circuit to a square wave current input should be like the one in fig.4.8a, that is the input signal derivative for a critically damped system. Actually the circuit is not a perfect second order and the response should be more like fig.4.8b, with an undershoot of 15% of A.

Monitoring with an oscilloscope the answer while a square wave input is given to the CTA module and changing R and L, it is possible to reproduce fig.4.8b, the optimum answer. Of course the transfer function depends also on the flow velocity, u, and this test has to be done at the maximum expected velocity.

When the right shape is reached, the limiting closed loop answer frequency is given by eq.4.4.

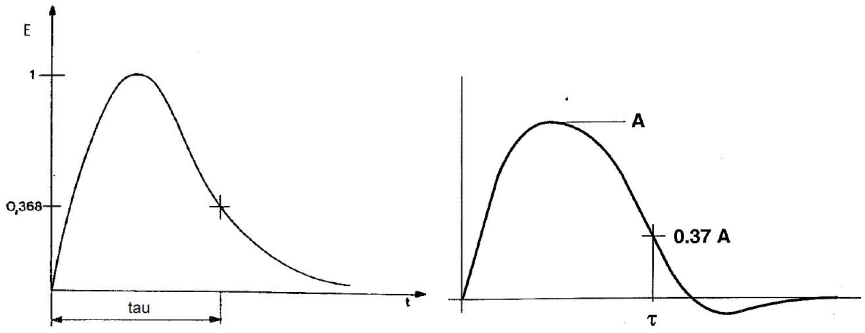

(a) Theorical answer. (b) Real answer.

Figure 4.8: Control circuit answers to a square wave input.

$$f_{\max}[Hz] = \frac{1}{2.02\tau[s]} \tag{4.4}$$

This give the frequencies shown in tab.4.8.

Probe number	**Maximum frequency**
1	15 kHz
2	10 kHz
3	14 kHz
4	30 kHz
5	30 kHz
6	30 kHz

Table 4.8: Limiting answer frequency.

4.4.2 Calibration facility

To calibrate the probe it was needed a facility in which both the flow total pressure and the total temperature could be modified. This facility is shown in fig.4.10.

It is worth to note also the device that allows to vary the probe pitch and yaw angle, see fig.4.11. This tool will be employed to analyze the probe angle sensitivity.

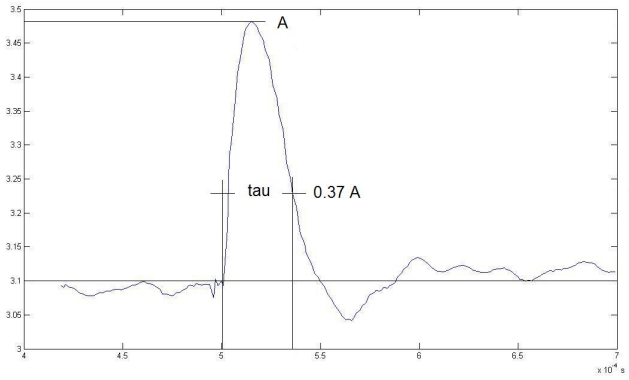

Figure 4.9: Head 3: example of square wave test result.

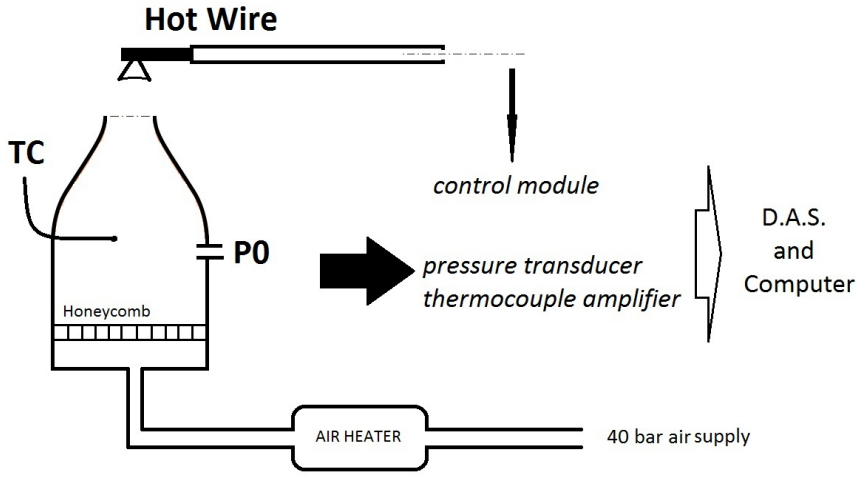

Figure 4.10: Schematic view of calibration facility.

4.5 Angle sensitivity analysis

The last problem considered during the calibration is the angle sensitivity. The probe is a single wire type and it is impossible to measure the angle with this type of probe; however between the measurements done there is the flow angle evaluation[11]. Once the angle is known it is possible to evaluate the true value of the velocity, fig.4.12.

With reference to fig.4.12, while the effect of u_x and u_z is the same, being the wire comparable with a cylinder and so with symmetry around the axis (parallel to y axis), u_y has a smaller influence on the wire cooling. In the

[11]This type of measure is done with the *five holes probe*.

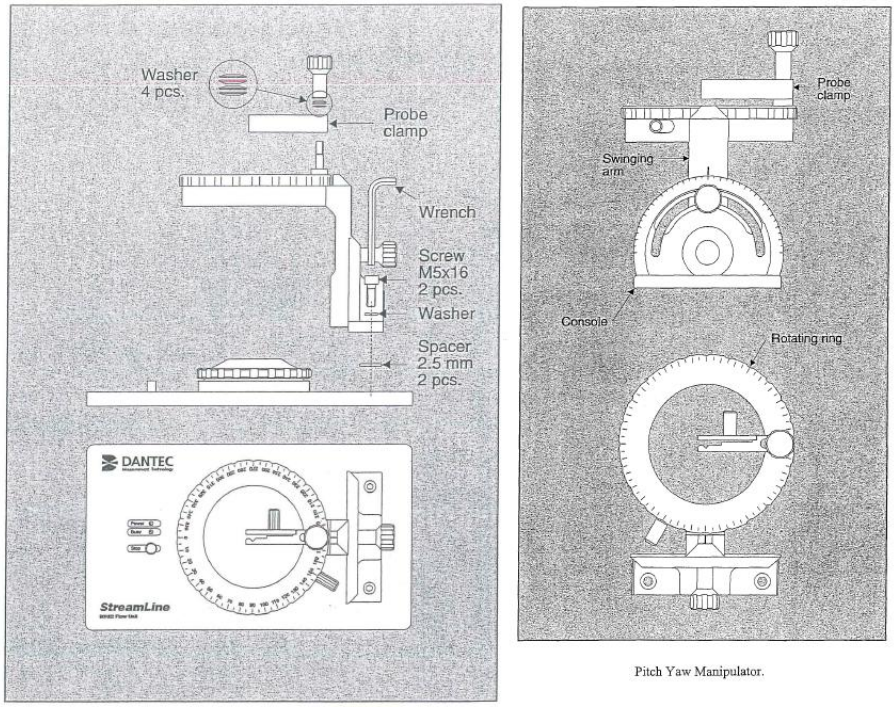

Figure 4.11: Hot wire angular regulator.

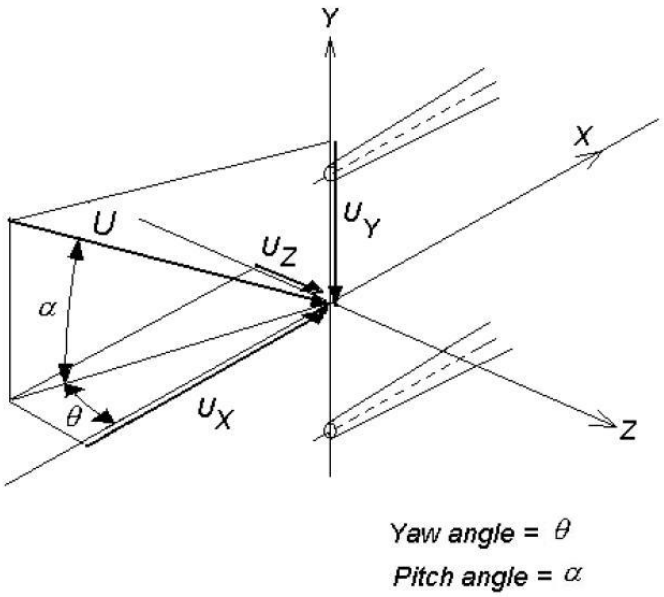

Figure 4.12: Scheme of pitch and yaw angles.

most part of the cases[12] the effect of u_y is negligible; this means that the voltage output, that is linked to u_{eff}, gives the velocity in $x - z$ plane and the real velocity is evaluable with the equation 4.5[13].

$$u_{\text{real}} = \frac{u_{\text{eff}}}{cos(\alpha)} \tag{4.5}$$

To be sure that the theory is applicable with the rake used, the effective velocity at different pitch angles is measured, from that the real velocity is calculated with eq.4.5 (being α known). Modifying the pitch angle, the voltage changes and the resulting effective velocity/voltage couple overlaps the calibration curve, fig.4.13; this means that the theory approximations can be used. Actually the fig.4.13 shows that, for the chosen probe design, this is true only for negative pitch angles, but in the experiments the expected value of pitch angle is negative.

4.6 Conclusion

Given the calibration curves with the corresponding application fields it is possible to go on with the core of the research: the *experimental investigation*. During that phase the hot wire anemometry will be used to analyze the flow turbulence intensity especially in relation with the differences between the various heat exchanger types employed.

[12] The effect of u_y has a not negligible influence when α tends to 90 deg and the cylinder axis is almost parallel to flow direction, but this is not the case of these experiments.

[13] The probe during the test is put in a way to minimize the yaw angle and so u_z, while the pitch angle cannot be controlled. If the effect of u_y on the output voltage is negligible u_{eff} is almost equal to u_x.

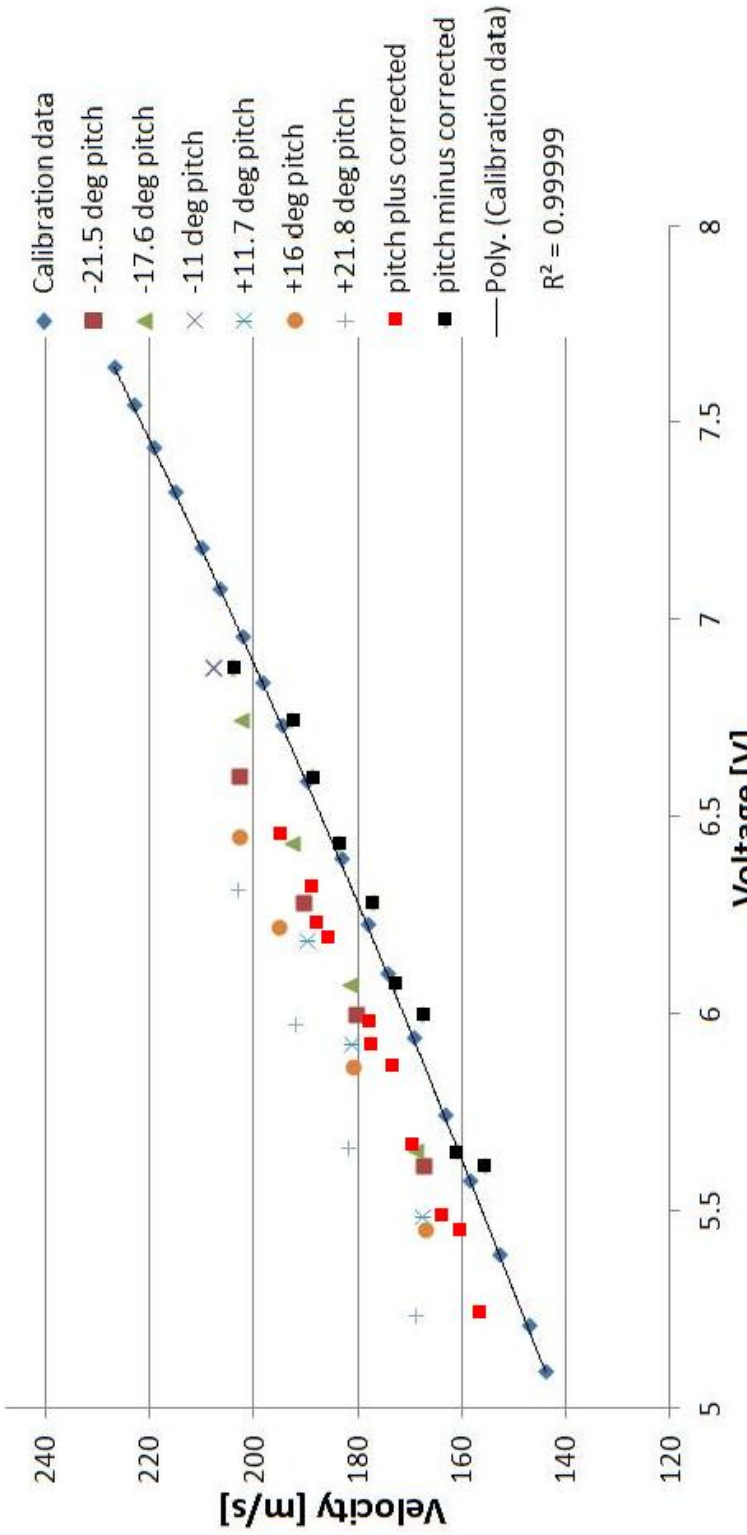

Figure 4.13: Hot wire 6 calibration curve, data at different pitch angles and effective velocity values.

Part II

Experimental investigation

Chapter 5

Flow analysis

In this chapter first the total temperature and then the turbulence data are analyzed; for each type of measure the contour maps are shown and the noise analysis is performed. At the end the principal achievements are listed.

5.1 Total Temperature

For each point of the measurement grid, see section 1.2.2, the data of the four thermocouple rake heads were acquired with a frequency of 1 kHz for 1 s. Simultaneously also the inlet total temperature time evolution in plane 0 was recorded with the same acquisition frequency and time.

All the signals were filtered using a digital second order low pass filter with cutting frequency $f_c = 40$ Hz, see also 5.1.3.

5.1.1 Mapping procedure

After the voltage/temperature conversion of each signal with the appropriate calibration data and the signal filtering and averaging, an appropriate reference total temperature value was used to make non-dimensional each rake head signal[1], see eq.[2].(5.1).

$$f = \frac{\overline{T}_T}{\overline{T}_{T\text{ref}}} \tag{5.1}$$

[1]Instead of non-dimensionalizing the rake signal with the reference and only after to average the ratio in each point, it was chosen to average the total temperature signal of both the rake and the reference signal and after to non-dimensionalize.

[2]The temperatures are in K.

Temperature analyses are presented in terms of temperature ratios due to the variation of the flow inlet temperature with time as the deposit is discharged. A characteristic value of the maximum inlet ΔT_T observed during a test is between $2 - 5$ K.

In the construction of the reference signal it was followed the temporal evolution of a probe that measures the central part of the considered plane during all the duration of each test (STT1 or 2 depending on the case). The middle portion of the section is not influenced by fins or boundary layer effects.

For each plane and probe geometry, the complete map was constructed interpolating the scattered data with a triangulation.

An example of the scatter with the resulting triangulation is shown in fig.5.1.

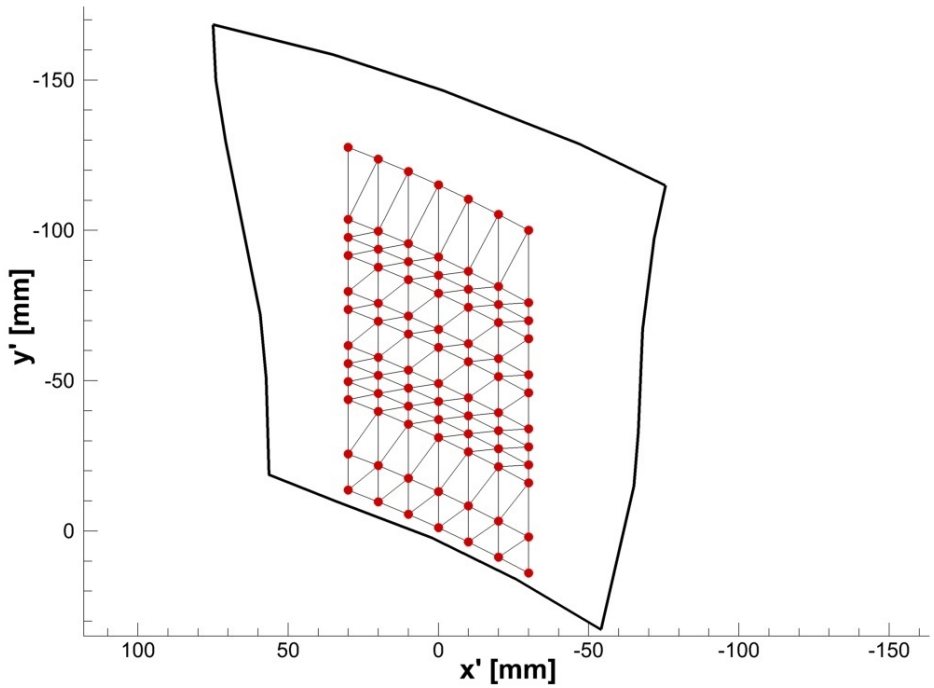

Figure 5.1: Plane 2 measurement points and triangulation mesh.

5.1.2 Plane 2, 3 and 4 maps

Analyzing the different total temperature maps in plane 2, just upstream the splitter, not significant differences are present between the configuration

without heat exchanger and the two other finned configurations (with continuous and interrupted fin heat exchanger) shown in fig.1.11. An example of total temperature ratio map[3] in plane 2 is given in fig.5.2.

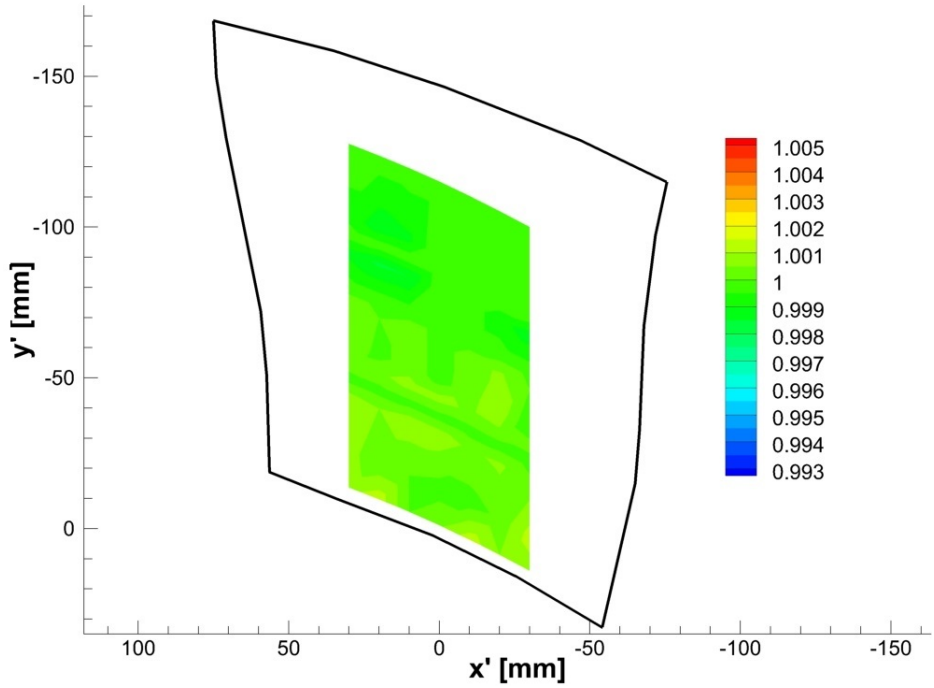

Figure 5.2: Plane 2 non-dimensional total temperature map with continuous fin heat exchanger.

In plane 3, just upstream the heat exchanger, the same conclusions as in plane 2 are achieved. The non-dimensional total temperature is uniform in the section regardless the configuration. The map inhomogeneities are still inside the measure uncertainty evaluated in chapter 6, that is $0.2 - 0.8$K or similarly $0.1 - 0.3\%$ of f, see fig.5.3.

Finally analyzing plane 4, downstream the heat exchanger, fig.5.4, it is possible to note that between the clean, fig.5.4a, and the continuous fin configuration, fig.5.4b, the differences are still inside the total temperature uncertainty margin with a maximum $\Delta f = 0.003$; while the presence of the interrupted fin heat exchanger causes a maximum Δf in the lower part of the section of 0.005 respect to the nominal uniform condition in which $f = 1$. This variation corresponds to a T_T decrease of 1.4K.

[3]Note that in all the section the maps have the same color scale, except where expressly stated.

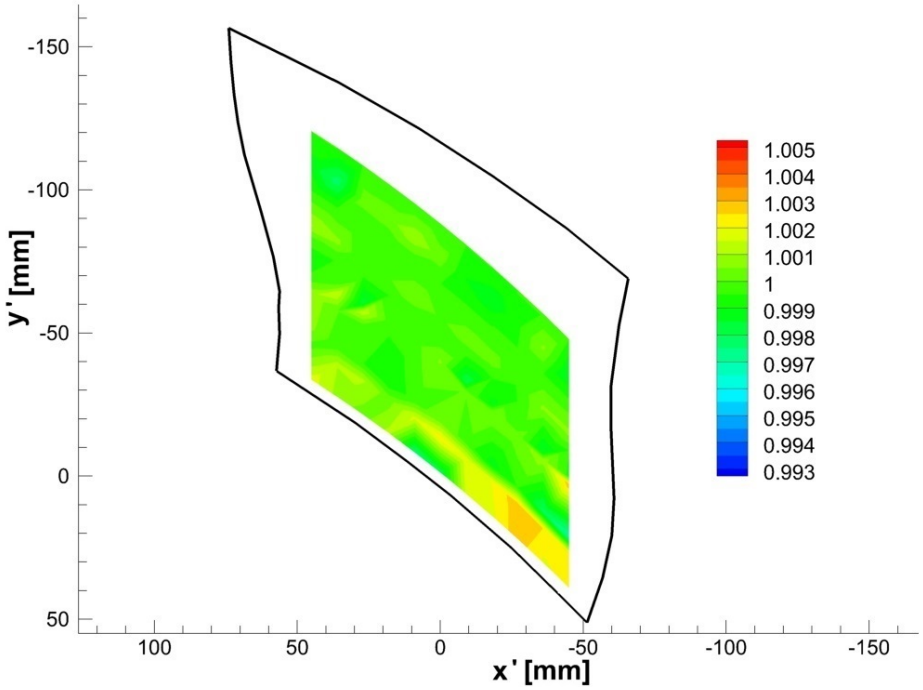

(a) Continuous fin configuration.

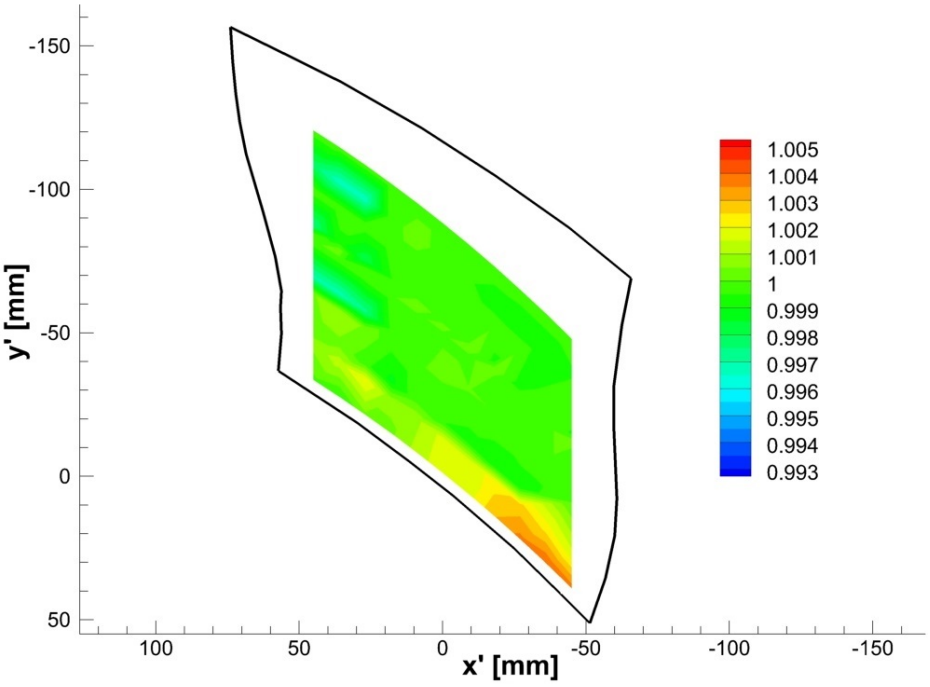

(b) Interrupted fin configuration.

Figure 5.3: Plane 3 non-dimensional total temperature maps.

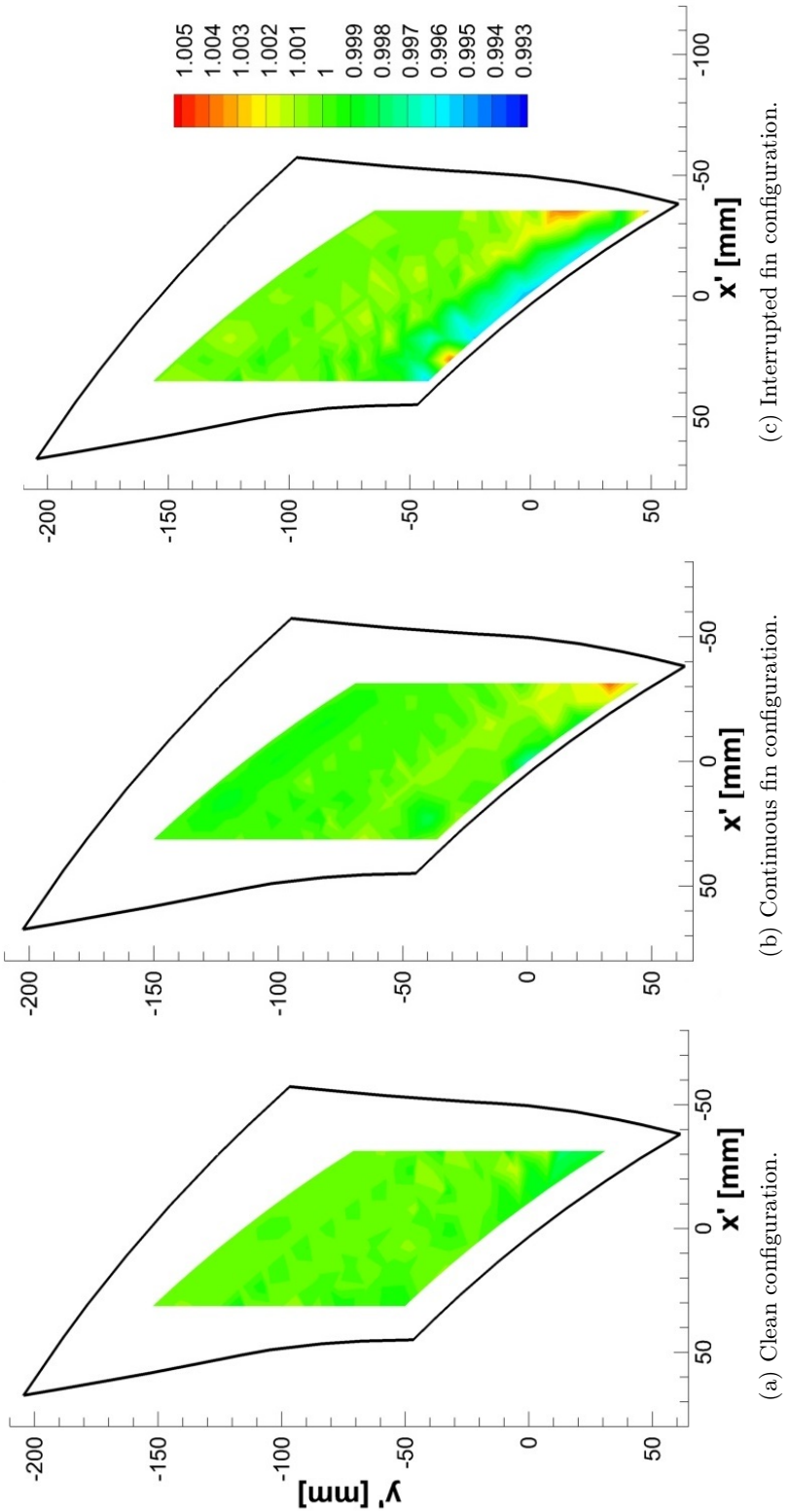

(a) Clean configuration. (b) Continuous fin configuration. (c) Interrupted fin configuration.

Figure 5.4: Plane 4 non-dimensional total temperature maps.

Focusing the attention on the central part of the section 4 in the proximity of the bottom wall (and changing the scale of the color map to underline the differences), fig.5.5, it is possible to note the heat exchanger zone of influence. It produces an extended lower temperature region in the case with interrupted fins, fig.5.5b.

In the case of continuous fins the differences are less marked but the heat exchanger wakes can be observed, fig.5.5a. The result is coherent with the turbulence measurements presented in the following section, see fig.5.15, but it was not expected with the total temperature measurement. This phenomenon was studied by *Bennet et al.* [20] and by *Gostelow and Carscallen* [21], which observed an energy stratification in the wake of a body in a high subsonic or transonic flow creating entropy and diminishing the flow total enthalpy.

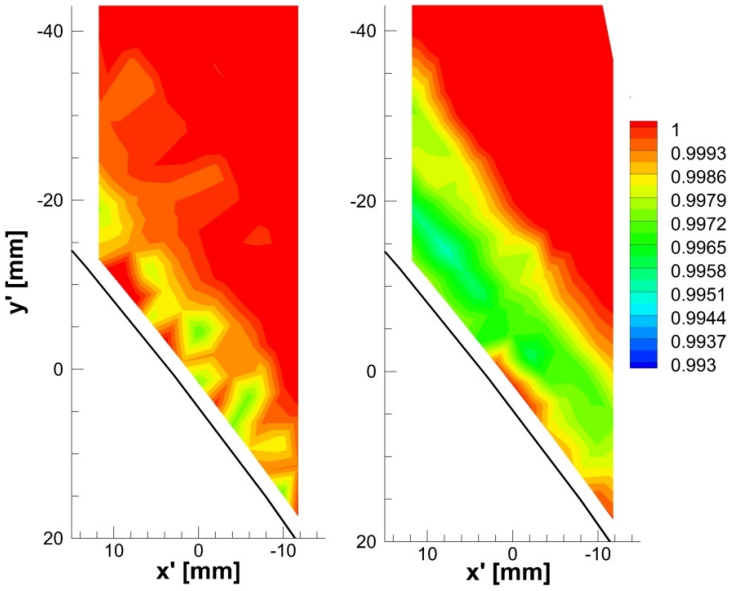

(a) Continuous fins. (b) Interrupted fins.

Figure 5.5: Plane 4 non-dimensional total temperature maps in the central zone with fine grid.

It is possible to conclude that the continuous fin configuration has a negligible influence on the total temperature field with a maximum difference of $\Delta f = 0.3$, that is equivalent to about a ΔT_T of 0.8K, equal to the maximum uncertainty on the measurement. Conversely the interrupted fins create total energy losses, decreasing the total temperature up to 1.4K in

	Peak to peak variation [V]	$\sigma \cdot 10^{-3}$ [V]
Calibration	0.076	9.7
Test without filter	0.197	32.1
Test with filter	0.108	13.6

Table 5.1: Noise during calibration and tests of STT2 (the reference test is plane 4 continuous fin configuration).

the lower part of the section downstream the heat exchanger.

5.1.3 Noise analysis

The previous maps are obtained filtering the raw signal with a *Butterworth*[4] low pass digital filter of order two and with a cutting frequency at 40 Hz to reduce the noise level; indeed analyzing the typical frequency content of a thermocouple, see fig.5.6b, three types of noise are recognized:

1. 50 Hz electrical noise. The noise peaks are broader during the tests because of the presence of a wider number of electrical devices in the facility respect to the calibration site and specially due to the two engine systems moving the probe;

2. white noise caused by the flow turbulence during the tests;

3. pink noise[5] due to the probe vibrations. The transonic Mach number in the test section gives rise to the probe vibration.

Most part of the tests was done using the probe STT6 to record the inlet temperature, for this reason in the following analysis this probe is analyzed; while between the rake heads it is chosen STT2. The other probes or rake heads have a similar behavior, remembering that each amplifier channel introduces a different level of noise as it is explained in subsection 2.3.2. At the end of the subsection a summary table with all the probe is given, tab.5.3.

It is clear that the test noise level is higher respect to the calibration one, so the two situations are compared in the follow.

[4]The Butterworth filter is a type of signal processing filter designed to have as flat a frequency response as possible in the passband.

[5]Pink noise is a signal or process with a frequency spectrum such that the Power spectral density (PSD) is inversely proportional to the frequency.

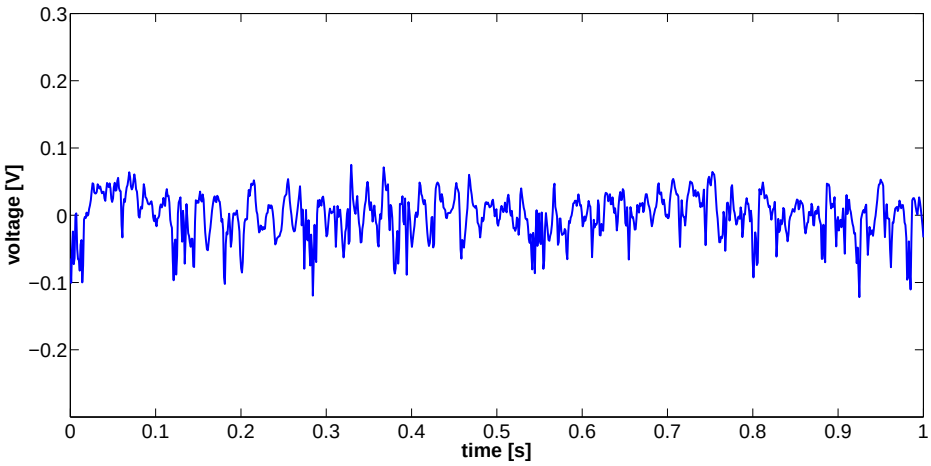

(a) Peak to peak variation.

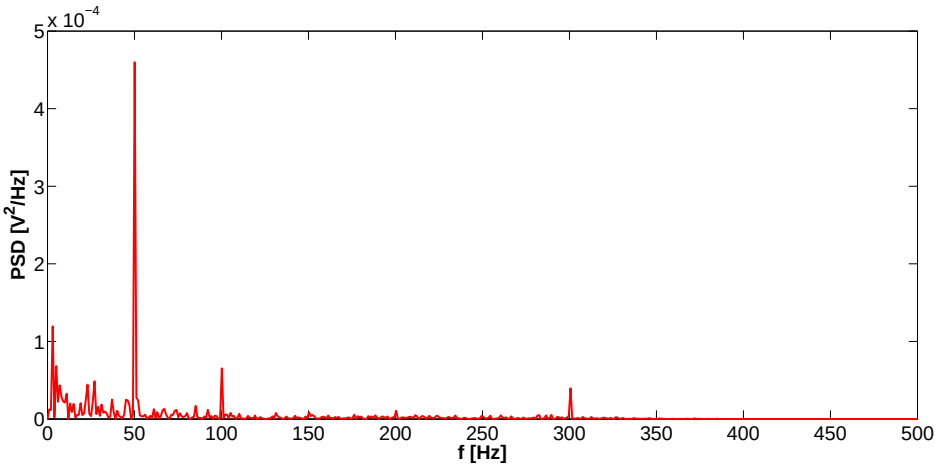

(b) Frequency content.

Figure 5.6: STT2 noise level in plane 4 with continuous fin configuration.

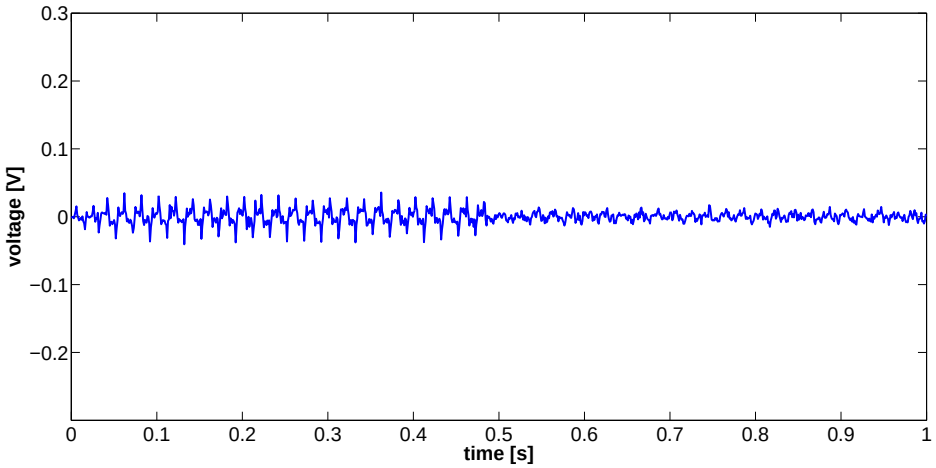

(a) Peak to peak variation.

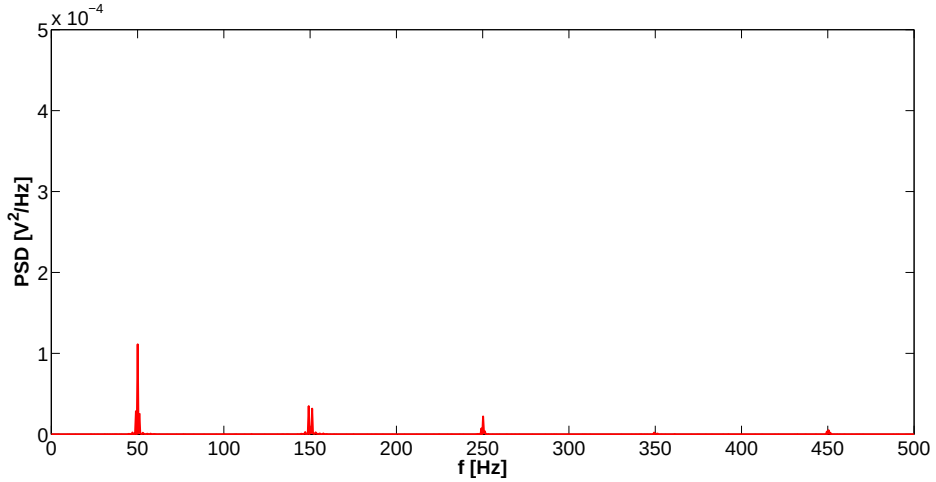

(b) Frequency content.

Figure 5.7: STT2 noise level during calibration.

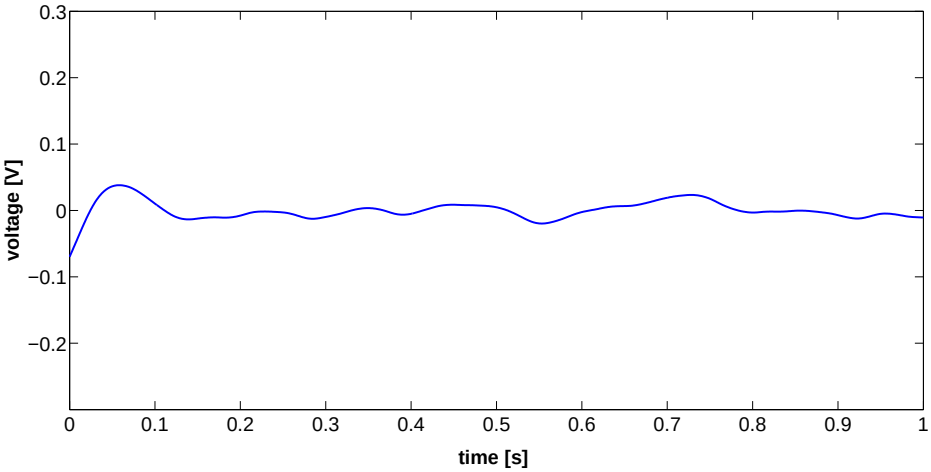

(a) Peak to peak variation.

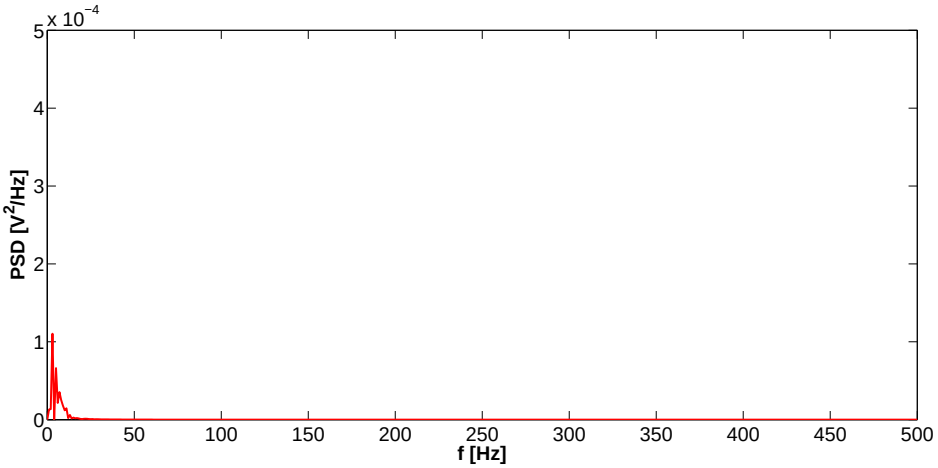

(b) Frequency content.

Figure 5.8: STT2 noise level in plane 4 with continuous fin configuration after filtering.

	Peak to peak variation [V]	$\sigma \cdot 10^{-3}$ [V]
Calibration	0.053	7.6
Test without filter	0.423	85.2
Test with filter	0.121	12.7

Table 5.2: Noise during calibration and tests of STT6 (the reference test is plane 4 continuous fin configuration).

STT2 analysis

Referring to the figures 5.6 and 5.7 it is possible to see how the probe vibration during the test increases both the standard (or RMS) deviation, σ, and the peak to peak variation of the test signal. Also the 50 Hz peaks are higher as previously said. The filter allows to reduce significantly the voltage oscillation, making the signal much more smoother, see fig.5.8, and cuts all the peaks that are the principal causes of the signal oscillations without interfering with the low frequency temperature variations in time. The table 5.1 summarize the STT2 noise analysis data.

STT6 analysis

The STT6 has the same type of behavior of the head 2 as shown in fig.5.9, 5.10 and 5.11, but it is worth to note the higher entities of the 50 Hz peaks during the test respect to the STT2 ones, compare fig.5.6b and 5.9b, while during the calibration it does not happen. The explanation is probably connected to the different location inside the test facility between the STT2 (in the measure plane) and STT6 (at the inlet) that leads the probe 6 to be more affected by the electronic noise.

For similar analysis on the other reference probes used (STT0 and STT7) see tab.5.3[6].

[6]In the table the continuous fins bis configuration is mentioned. It is a configuration still in which the heat exchanger has continuous fins, but with the possibility to be heated up with a power supply (this report does not deal with the fin heating).

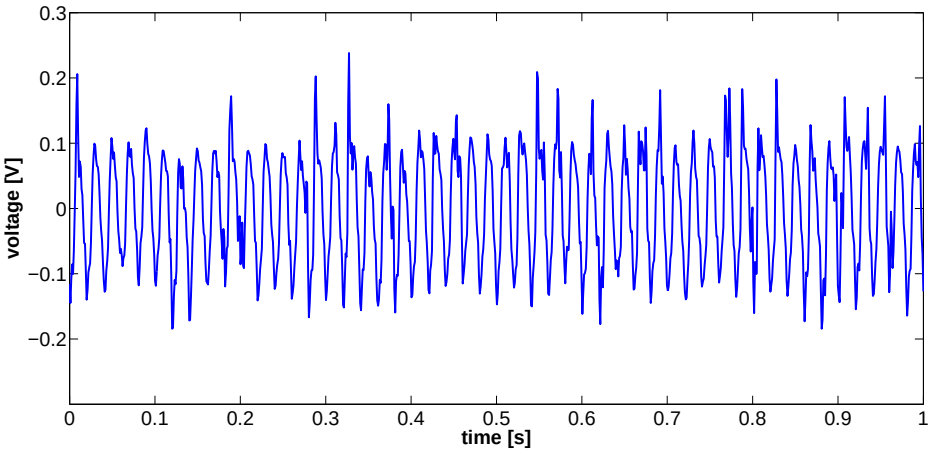

(a) Peak to peak variation.

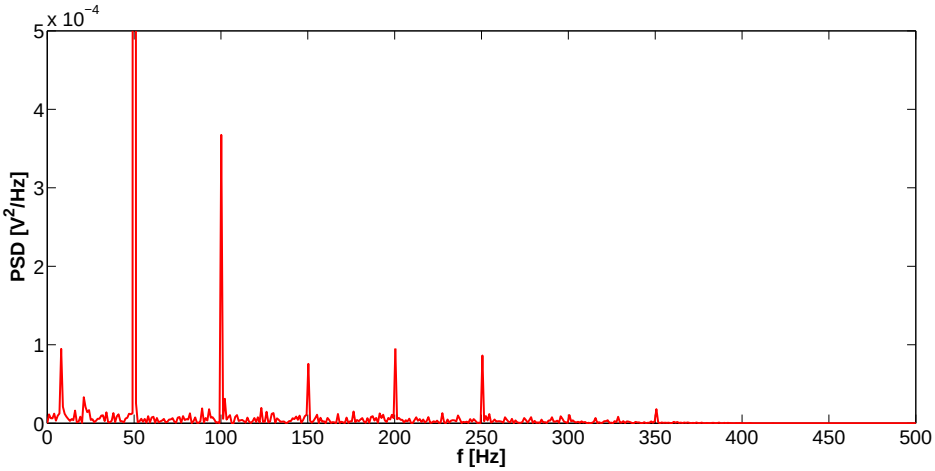

(b) Frequency content.

Figure 5.9: STT6 noise level in plane 4.

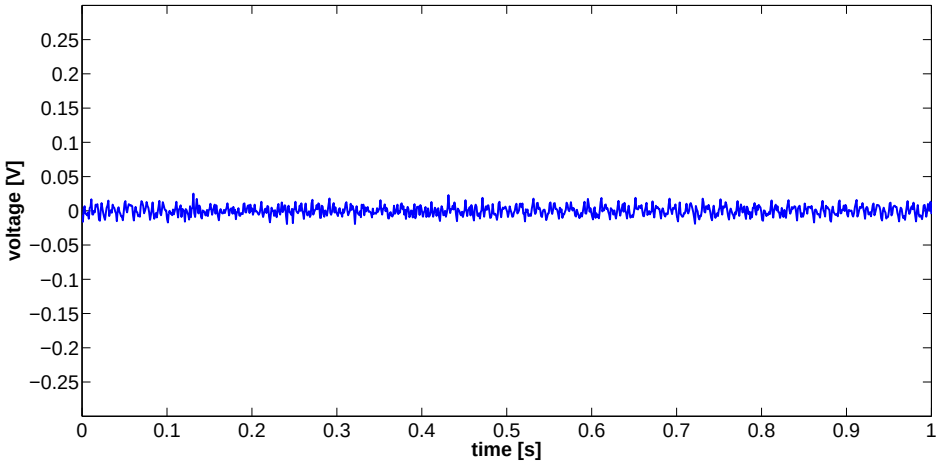

(a) Peak to peak variation.

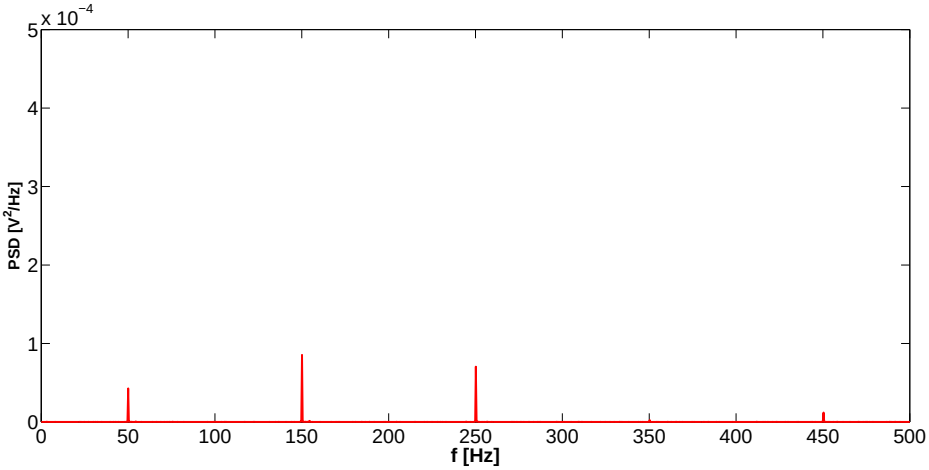

(b) Frequency content.

Figure 5.10: STT6 noise level during calibration.

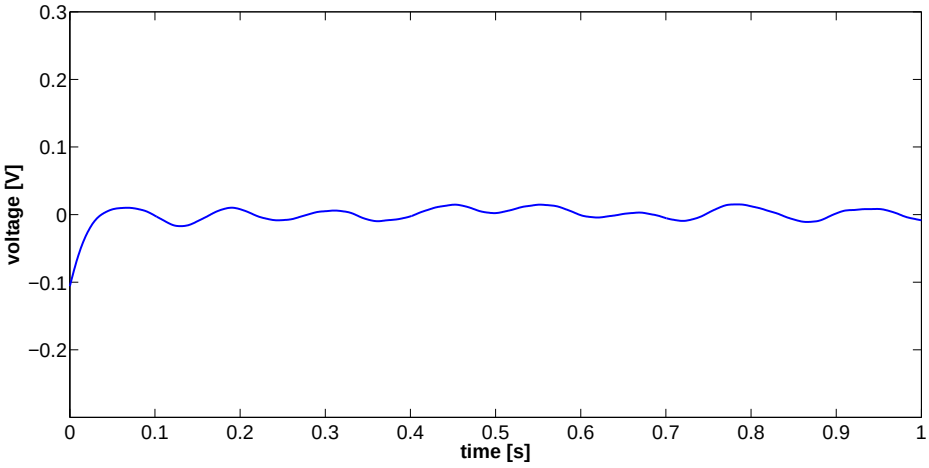

(a) Peak to peak variation.

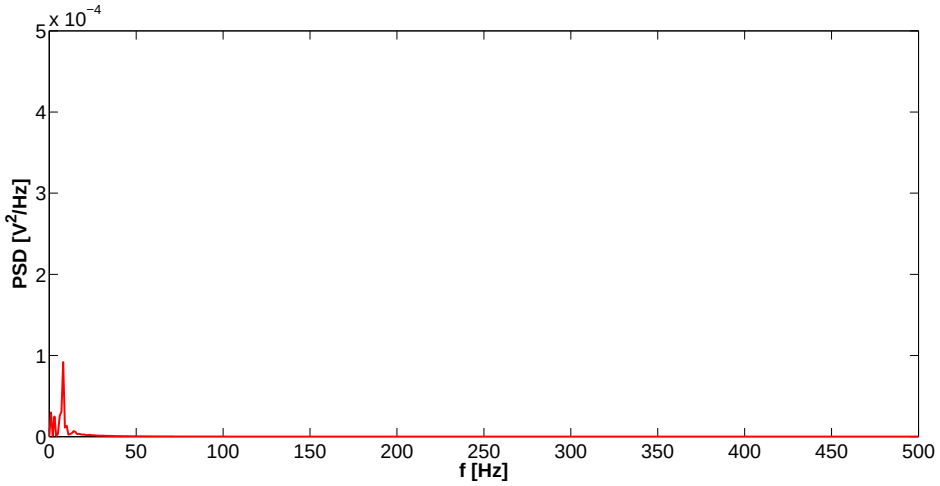

(b) Frequency content.

Figure 5.11: STT6 noise level in plane 4.

	STT	Peak to peak variation [V]	$\sigma \cdot 10^{-3}$ [V]
Calibration	1	0.051	7.3
	4	0.033	4.8
	5	0.036	4.7
	7	0.030	4.7
	0	0.148	37.2
Tests	1	0.292	41.6
	4	0.132	20.6
	5	0.231	37.4
	7	0.524	83.5
	0	0.355	71.6

Table 5.3: Noise during calibration and tests for the other probes without filtering. The reference test is plane 4 continuous fin configuration for head number 1, 4 and 5, while plane 4 continuous fins bis for the STT0 and finally plane 4 interrupted fins for the STT7).

5.2 Turbulence

As it was explained in chapter 4, each hot wire probe head allows to measure the effective velocity, u_{eff}. Given this information it is possible to evaluate the turbulence intensity, Tu, per each measurement point, see eq.(5.2).

$$Tu = \frac{u_{\text{RMS}}}{\overline{u}} \tag{5.2}$$

$$u_{\text{RMS}} = \sqrt{\frac{\sum_1^N (u - \overline{u})^2}{N - 1}} \tag{5.3}$$

where u_{RMS} is the RMS velocity defined in the eq.(5.3) and $\overline{u}$ is the mean velocity in the considered point; both u_{RMS} and $\overline{u}$ are evaluated on the basis of the real velocity, u_{real}:

$$u_{\text{real}} = \frac{u_{\text{eff}}}{cos\,(\alpha)} \tag{5.4}$$

calculating Tu the factor $cos\,(\alpha)$ is canceled out, any angle correction is not necessary for the turbulence mapping.

Before the test section the honeycombs control the inlet turbulence level, measured in plane 0 (without probe traversing) obtaining a mean value of 0.02, or alternatively 2%.

The acquisition time in each point is 1 s with a sampling frequency $f_s = 90$ kHz.

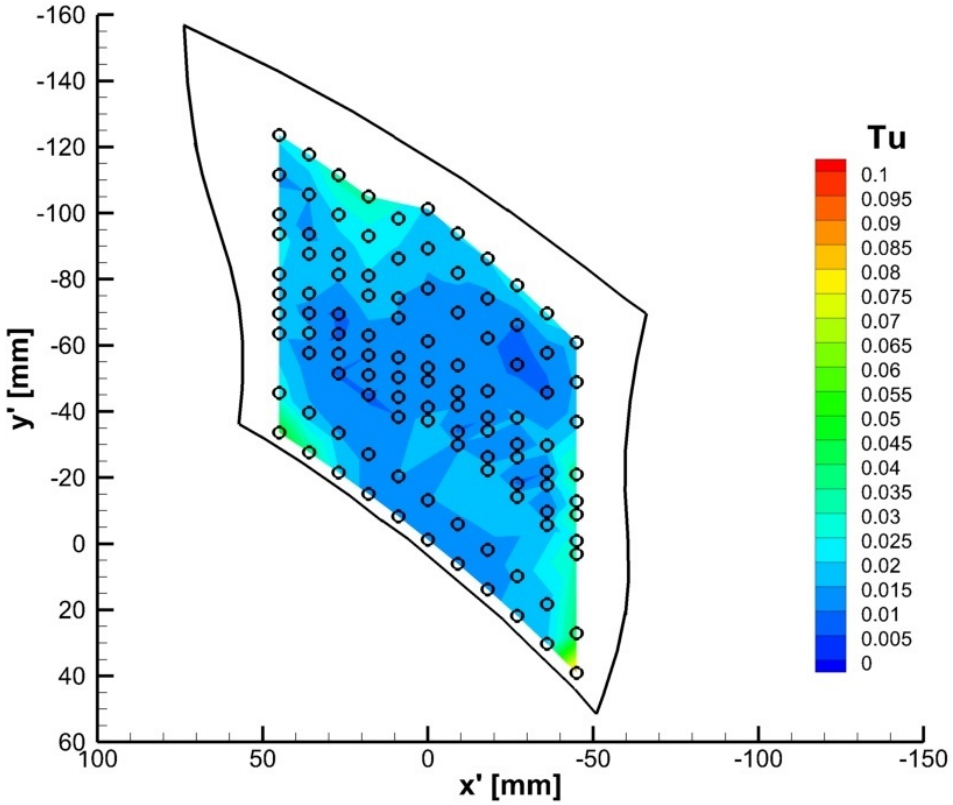

Figure 5.12: Plane 3 turbulence intensity (clean configuration).

5.2.1 Mapping

To analyze the influence of the heat exchanger presence and type, the analysis starts from a reference turbulence map, fig.5.12. It refers to the turbulence intensity before the heat exchanger location, plane 3 in the *clean* configuration. In the figure it is worth to note a mean turbulence level of 0.02 with two peaks corresponding to the bottom corners due to the interference of the lateral wall with the bottom wall boundary layers.

The interpolation of the data follows the method applied for the thermocouples data analysis and the following turbulence maps have the same color scale of fig.5.12 (except where expressly stated), to underline the differences between the analyzed configurations. In the aforementioned figure also the measurement points locations are plotted (the small black circles), while in

the next plots only the maps are presented.

Comparing fig.5.12 and 5.13 it is seen an increase of the turbulence intensity in the lower part of the wind tunnel even in the *clean* configuration up to a level of 0.05, this is due to the boundary layer that develops along the bottom wall.

It is worth to note, taking into account the differences between fig.5.13a and 5.13b, how the continuous fin configuration increases the turbulence level[7] respect to the *clean* configuration, but not significantly, ΔTu respect to the *clean* of about $0.5 - 1\%$; conversely the interrupted fins create an high turbulence level with a maximum ΔTu respect to the *clean* configuration of about $7 - 8\%$, see tab.5.4 and also fig.5.14. In this last figure in the bottom part of the section 4 it is possible to see the high turbulence region due to the heat exchanger, that extends for 30% of the section height[8] (instead of the 20% of the other two configurations) up to a maximum value of 0.15.

[7]The three tests (in the *clean* configuration and with continuous or interrupted fin heat exchanger in plane 4) were done at comparable Mach and Reynolds numbers.

[8]Computed in the y' direction.

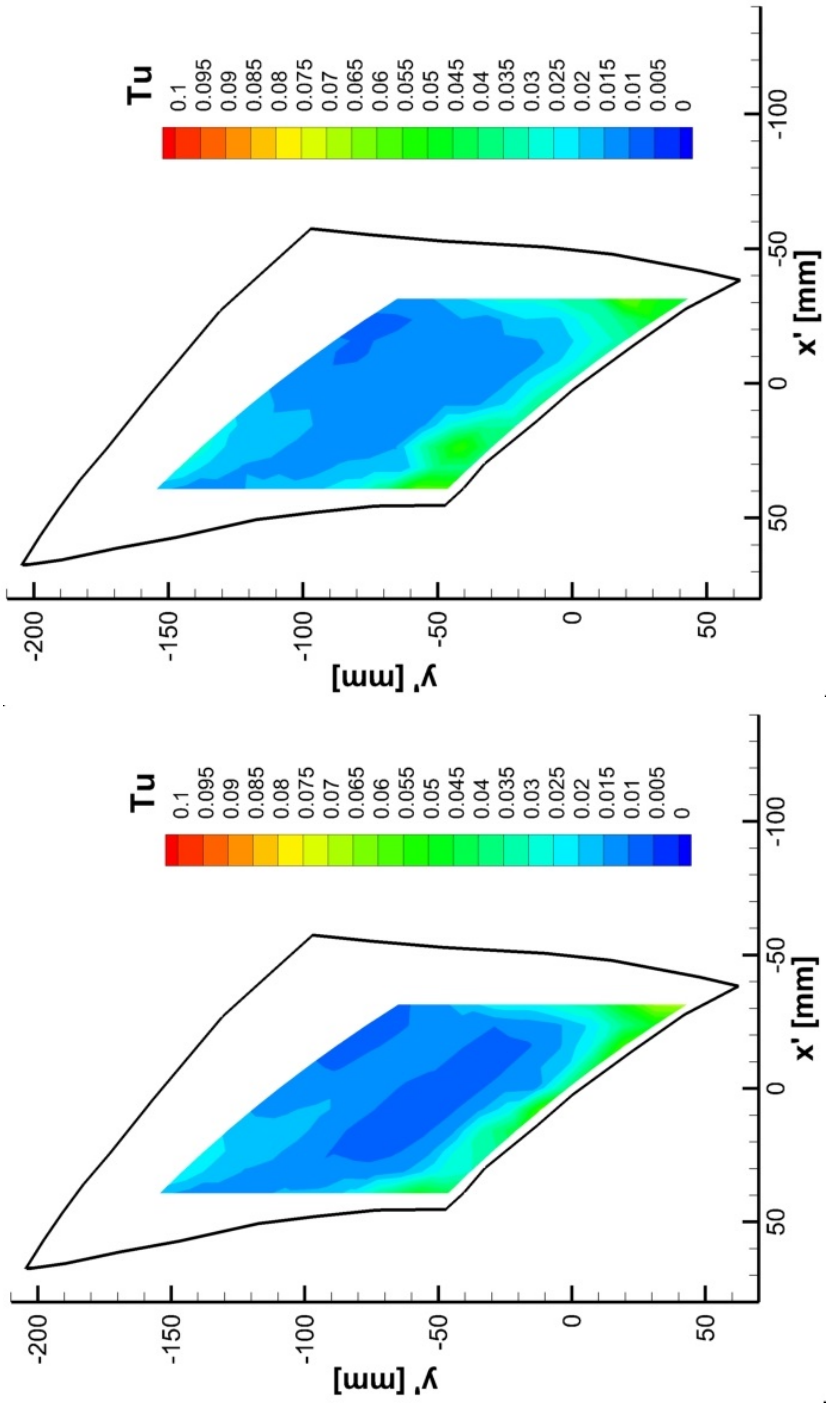

(a) Clean configuration.

(b) Continuous fin configuration.

Figure 5.13: Plane 4 turbulence map comparison (coarse grids).

	$\bar{\mathbf{Tu}}$ [%]
Clean	1.9
Continuous fins	2.1
Interrupted fins	3.7

Table 5.4: Mean turbulence level in plane 4 for different configurations.

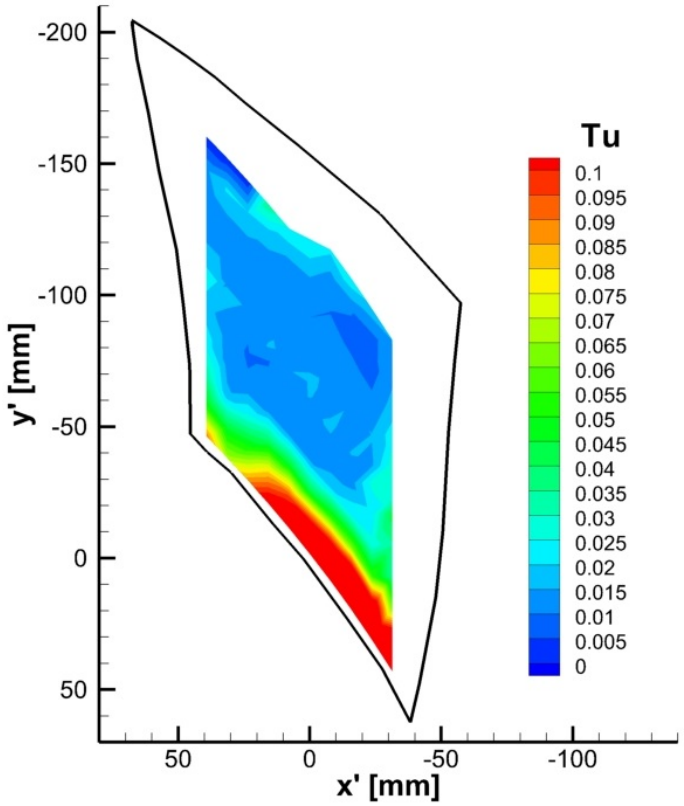

Figure 5.14: Plane 4 turbulence intensity map with the interrupted fin heat exchanger (coarse map).

Another peculiarity of the continuous fins turbulence maps is the presence of turbulence peaks in the bottom boundary layer region corresponding to the fin wakes, see fig[9].5.15 where the color scale is changed to underline the fin wakes. However the level of the peaks is negligible; in fact the difference between point A (turbulence peak region) and B of the map 5.15b is 0.01.

[9]The turbulence level of this test is slightly lower respect to the coarse grid done with the same configuration. This is due to the fact that the Mach and Reynolds number are slightly lower in this test, causing the turbulence decrease.

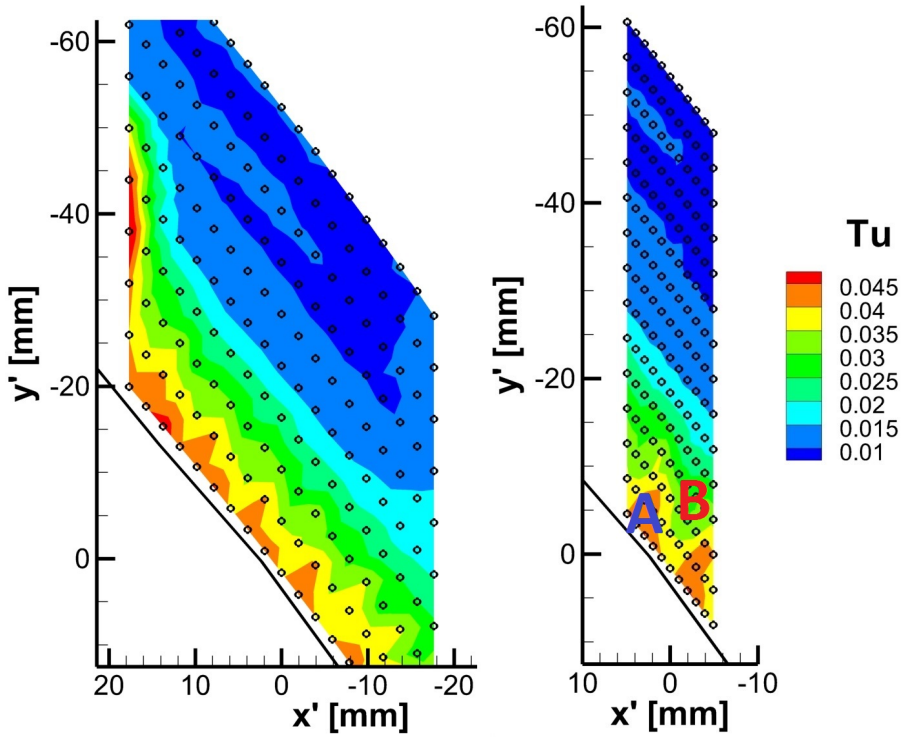

(a) Intermediate grid. (b) Fine grid.

Figure 5.15: Plane 4 continuous fin configuration turbulence maps details.

In plane 5 the turbulence diffuses making the bottom turbulent region more uniform, fig.5.16; in particular for the continuous fin configuration the fin wakes are not anymore recognizable, see fig.5.16b. The radial extent of the perturbations is still about 10% higher for interrupted fins compared to the *clean*; for the latter configuration the perturbed region height remains in the order of 20% of the total section height as well as for the continuous fin case.

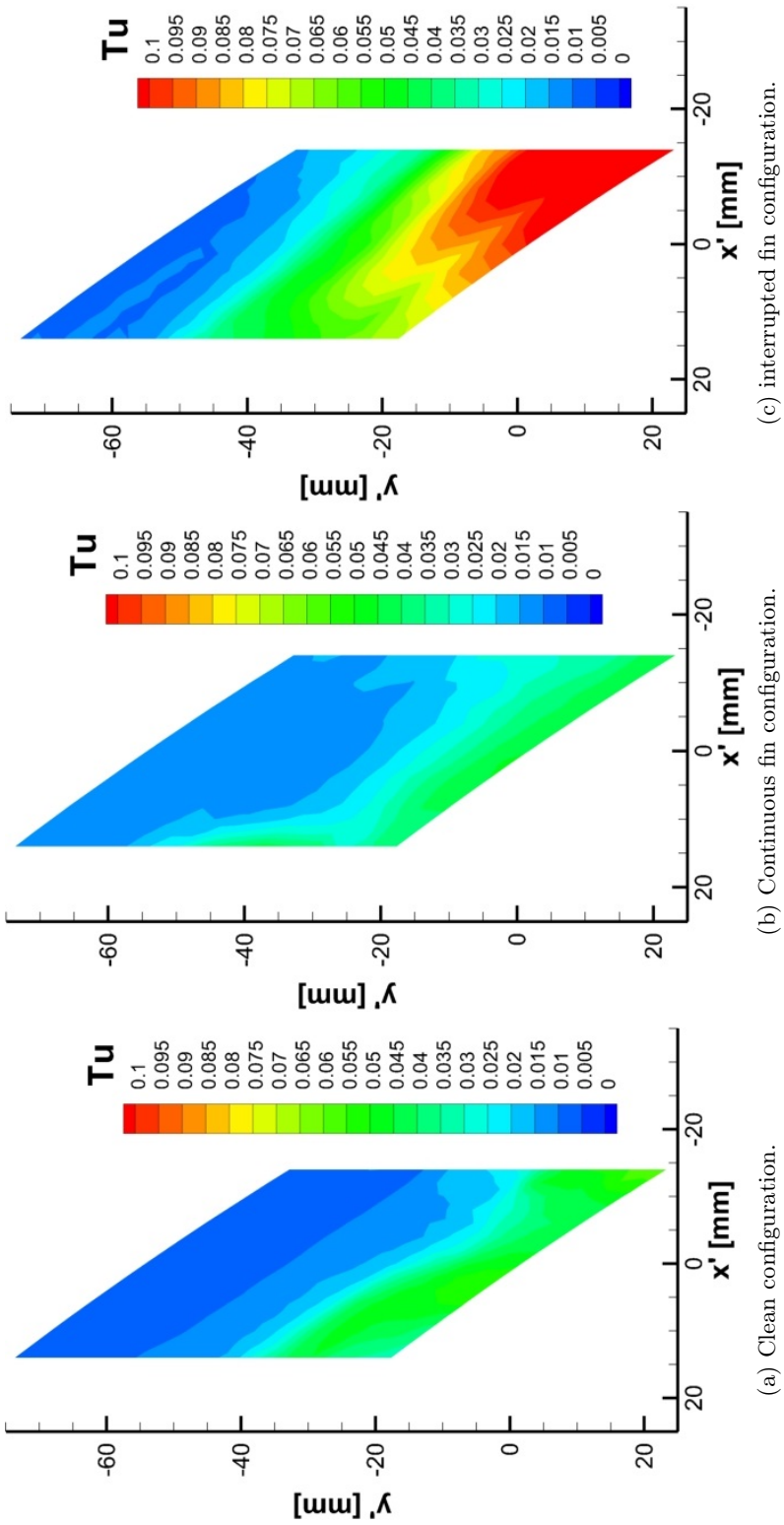

(a) Clean configuration. (b) Continuous fin configuration. (c) interrupted fin configuration.

Figure 5.16: Plane 5 turbulence map comparison (central part of the section).

5.2.2 Frequency content analysis

The previous maps were done filtering the raw signal, both the *VKI* and the *Dantec* control modules allow the setting of an analogical prefilter indeed. Considering the Nyquist-Shannon sampling theorem and the limitation on the maximum *VKI* module filter cutoff frequency, $f_{c\mathrm{MAX}} = 10$ kHz, the chosen f_c are shown in tab.5.5[10].

Probe	Cutoff frequency
HW1	10 kHz
HW2	10 kHz
HW3	10 kHz
HW4	30 kHz
HW5	30 kHz
HW6	30 kHz

Table 5.5: Hot Wire rake head filter cutoff frequency.

As indicated in table 5.5 the wires that are controlled by *Dantec* modules have a different f_c; in particular for hot wires 4, 5 and 6 the f_c is set at an higher value because of the higher response frequency of the *Dantec* boxes; that allows to have a major frequency content resolution of the velocity fluctuations, see tab.4.8.

A typical Power spectral density (PSD) is shown in fig.5.17 where wires 2 and 6 are compared taking two measurement points in the central part of the section, where the flow should have the same behavior. As it was expected the hot wire 6 resolves up to more than 30 kHz, while wire 2 up to 10 kHz. However the PSD peaks beyond 10 kHz are of lower entities and do not change significantly the turbulence level measured by wire 6 respect to number 2: the resulting map is uniform also in the central zone, where points in which the turbulence is measured with wires 5 and 6 overlap points taken with head 1 and 2, as it is shown in fig.5.14.

It is worth to note that all the frequencies beyond the prefilter cutting frequency are spurious and come from the facility noise affecting the control module output. The final acquired signal can be filtered with a fourth order *Butterworth* digital filter with a cutting frequency of 30 kHz. The result for wire 6 is shown in fig.5.17c and can be compared with fig.5.17b. Anyhow,

[10]The rake head number starts from the top head, HW1, to the bottom head, HW6.

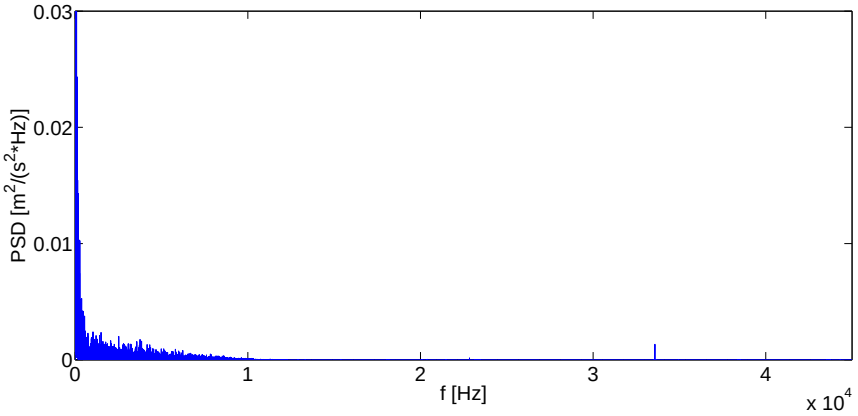

(a) Hot wire number 2.

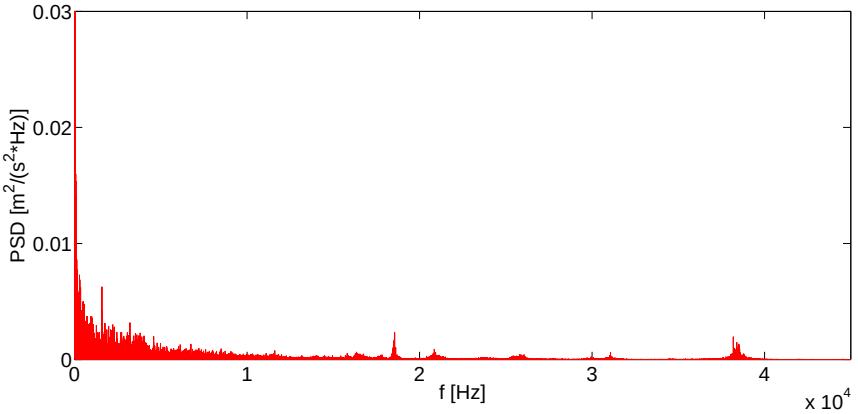

(b) Hot wire number 6.

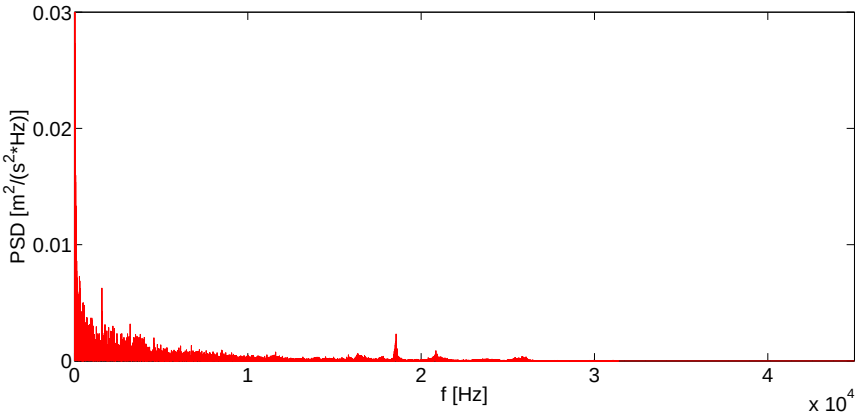

(c) Hot wire number 6 digital filtered with cutting frequency at 30 kHz.

Figure 5.17: Typical power spectral density (plane 4 interrupted fin configuration).

comparing the digital filtered map, fig.5.18, with the fig.5.14 (that is done only with the prefiltered signal), the turbulence level changes are negligible.

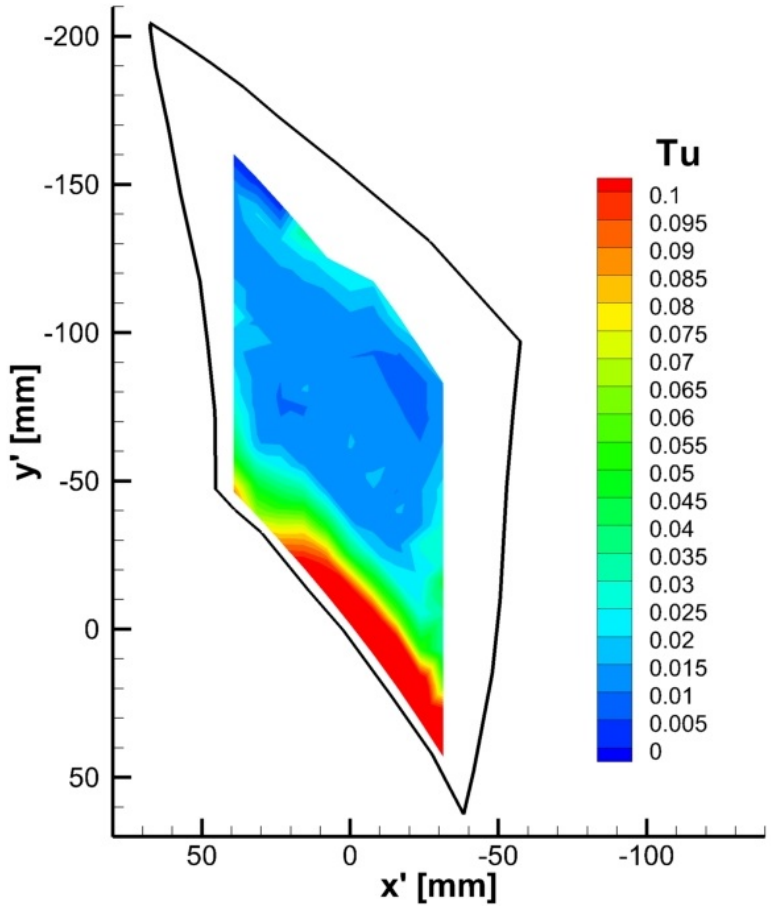

Figure 5.18: Plane 4 map in the interrupted fin configuration digital filtered, with cutting frequency at 30 kHz.

5.3 Conclusion

From the previous analysis it is possible to conclude that:

- from the point of view of the total temperature the heat exchanger configuration has a small influence. With the continuous fins the maps are uniform within the uncertainty level of the measurement, while with the interrupted fin heat exchanger a maximum $\Delta T_T = 1.4$K is measured.

- conversely the turbulence level changes significantly in the interrupted fin configuration, on the other hand the continuous fins influence is negligible respect to the *clean* configuration.

So regarding temperature and turbulence the integrated Air Cooled Oil Cooler (ACOC) with a continuous fin heat exchanger can be considered a good trade-off for cooling requirements with regard to the aerodynamic efficiency.

Chapter 6

Uncertainties analysis

The method used to estimate the uncertainty on the measurements is called *perturbation method* and states that the uncertainty on y (function of n independent parameters x_i, $y = f(x_1, x_2, ..., x_n)$) is estimated with the eq.(6.1)[1].

Each dx_i is the standard deviation of a direct measured quantity (with a confidence level of the 65%), or two times the standard deviation if a confidence level of the 95% is needed; while e_j are the uncertainties related with the errors not due to the direct measured variables, see the *Measurement techniques in fluid dynamics* [1] for further informations.

$$dy = \sqrt{\left(\frac{\partial y}{\partial x_1} dx_1\right)^2 + ... + \left(\frac{\partial y}{\partial x_n} dx_n\right)^2 + e_1^2 + ... + e_m^2} \tag{6.1}$$

6.1 Temperature ratio uncertainty

Given the expression in eq.(5.1) where f is function of $\overline{T}_T$ and $\overline{T}_{T\text{ref}}$, the uncertainty in the ratio can be expressed as:

$$df = \sqrt{\left(\frac{d\overline{T}_T}{\overline{T}_{T\text{ref}}}\right)^2 + \left(-\frac{\overline{T}_T}{\overline{T}_{T\text{ref}^2}} d\overline{T}_{T\text{ref}}\right)^2} \tag{6.2}$$

where for each total temperature uncertainty $d\overline{T}_T$ it was considered three error sources:

- the uncertainty in the voltage signal. The entity of this error changes from point to point, but especially from probe to probe. However the

[1] The equation neglects the Taylor expansion terms with an order higher than one.

value is in the range 0.1 − 0.6 K;

- the uncertainty due to the evaluation of the calibration temperature[2], that reflects to a final error of 0.1 K;
- the uncertainty due to the fitting of the calibration data. It has a value between 0.05 − 0.1 K.

The previous values lead to a maximum final $d\overline{T}_T$ in the range 0.2 − 0.8 K. It reflects into a *df* in the range 0.001 − 0.003, to have further details see the relative section in the appendix A.

6.2 Turbulence uncertainty

Regarding the turbulence it is worth to note that, to estimate the uncertainty level dTu, it is necessary only to evaluate the velocity uncertainty, du. Considering the three sources of uncertainties taken into account:

- the uncertainty in the voltage signal;
- the uncertainty due to the evaluation of the calibration velocity;
- the uncertainty due to the fitting of the calibration data;

it is possible to demonstrate eq.(6.3)

$$\frac{dTu}{Tu} = \frac{du}{u}\sqrt{2} \tag{6.3}$$

The previous relation is justified because the three sources of error spread in the same way both for the mean and for the RMS velocity (see also the reference *Alcune considerazioni sulla valutazione dell'incertezza nelle misure con anemometro a filo caldo* [22]) allowing to write

$$\frac{du}{u} = \frac{d\overline{u}}{\overline{u}} = \frac{du_{\mathrm{RMS}}}{u_{\mathrm{RMS}}} \tag{6.4}$$

but starting from the turbulence definition in the eq.(5.2) and using the perturbation method

[2]This type of uncertainty comes from the relative analysis of the bare type K thermocouples, used during the calibration of the STTs.

$$dTu = \sqrt{\left(\frac{\partial Tu}{\partial u_{\mathrm{RMS}}} du_{\mathrm{RMS}}\right)^2 + \left(\frac{\partial Tu}{\partial \overline{u}} d\overline{u}\right)^2} \tag{6.5}$$

and developing the partial derivatives

$$dTu = \sqrt{\left(\frac{u_{\mathrm{RMS}}}{\overline{u}}\right)^2 \left[\left(\frac{du_{\mathrm{RMS}}}{u_{\mathrm{RMS}}}\right)^2 + \left(\frac{d\overline{u}}{\overline{u}}\right)^2\right]}$$

that taking into account the relation (6.4) leads to (6.3).

6.2.1 Velocity uncertainty

The entity of the total velocity uncertainty, that includes the three aforementioned contributions, is function of the velocity itself.

The first (the voltage du) has the trend shown in fig.6.1a; while for the second (the uncertainty in the estimation of the calibration velocity) the fig.6.1b shows the evolution. This latter includes the uncertainty in measuring total temperature and total pressure, but also static pressure, respectively[3] 0.1 K, from 20 to 550 Pa and finally 20 Pa.

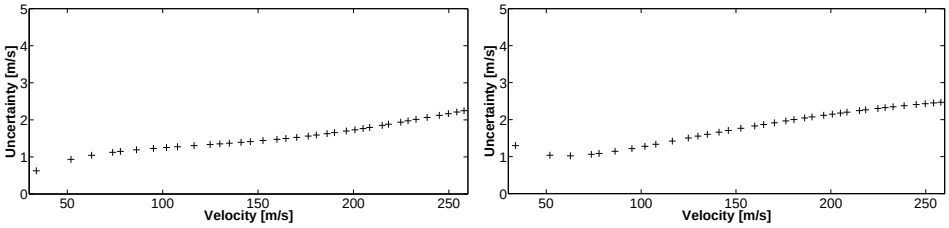

(a) Voltage contribution. (b) Calibration velocity contribution.

Figure 6.1: Main velocity uncertainty sources in the case of hot wire 5.

The voltage and the calibration contributions, together with a fitting uncertainty of 0.5 m/s, lead to the total uncertainty on the velocity, fig.6.2, and to the turbulence relative uncertainty dTu/Tu, fig.6.3a. See appendix A to have further details on the way of evaluating the uncertainties.

Repeating the procedure considering the hot wire number 2 (using a *VKI* control module) instead of the number 5 (using *Dantec* control module) as

[3]For the total temperature is a typical uncertainty value for bare type K thermocouples. Moreover for the total pressure it is worth to note that the total pressure uncertainty is typically 1% of the measured gauge pressure, see also *Measurement techniques in fluid dynamics*, [1]. This is why it increases with the Mach number.

in the previous analysis, it is worth to note an increase of the uncertainty level, see fig.6.3b.

It is important to underline the different velocity range considered for hot wire 2 (and the other wires using *VKI* modules) respect to number 5 (and the other wires using *Dantec modules*: 4, 5 and 6). This is due to the fact that the wires 4, 5 and 6 are used to analyze the lower part of each measurement plane, where the velocities are lower because of the presence of the boundary layer.

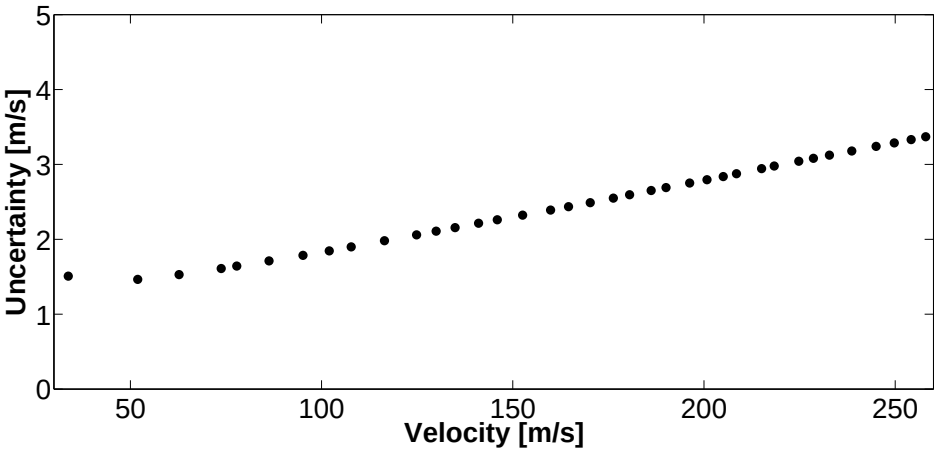

Figure 6.2: Total velocity uncertainty in the case of hot wire number 5.

6.3 Conclusion

Finally the obtained values of global uncertainties are between 0.1 and 0.3% of f for the non dimensional temperature ratio measure, and between 1 and 4.5% of Tu in the respective operational velocity range for the turbulence[4]. The uncertainty increases up to 5-15% of Tu if the hot wires that use *VKI* control circuit are considered, see fig6.3.

[4]The aforementioned values of turbulence uncertainty are relative the hot wires using the *Dantec* control module.

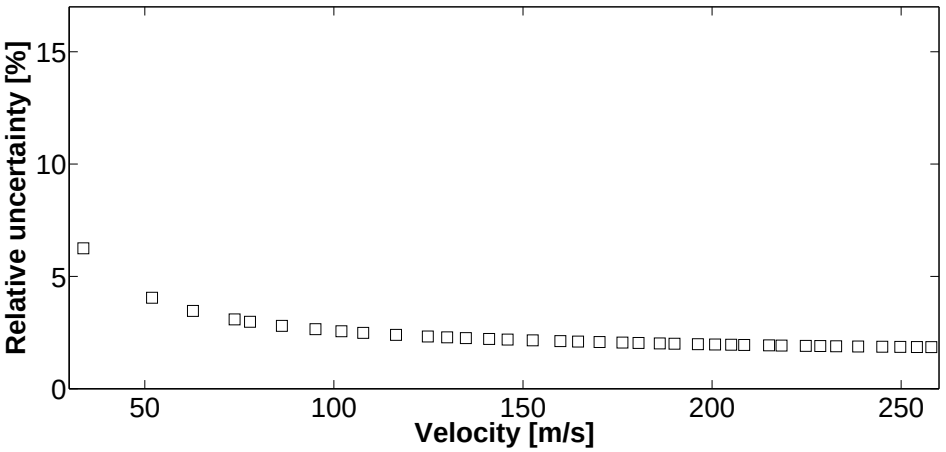

(a) Hot wire 5, controlled by Dantec circuit.

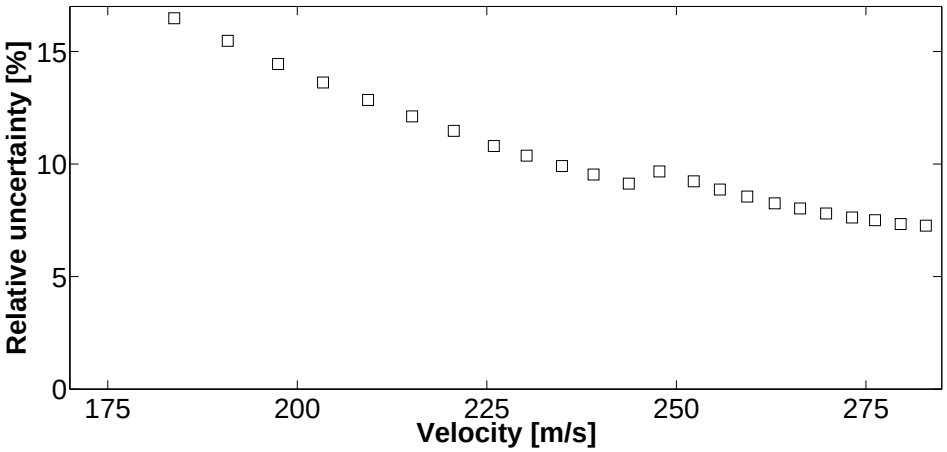

(b) Hot wire 2, controlled by VKI circuit.

Figure 6.3: Turbulence relative uncertainty.

Part III

Conclusion

Chapter 7

Conclusion and further investigations

7.1 Conclusion

In the present work total temperature and turbulence measurements in a transonic wind tunnel were performed. The purpose of the research was to investigate the aerodynamic behavior of the bypass flow in an high bypass ratio turbofan if an Air Cooled Oil Cooler (ACOC) heat exchanger is introduced just after the splitting of the inlet flow.

The results listed in chapter 5 show how the type of heat exchanger influences the flow total temperature and turbulence.

Regarding the turbulence, Tu, negligible differences between the presence of the continuous fin heat exchanger or the *clean* configuration are measurable; a maximum ΔTu of 1% is measured in plane 4 between the two cases, and the radial perturbation caused by the bottom wall boundary layer in plane 4 and 5 remains in the order of 20% of the section height for both configurations. A significant difference is present between the turbulence measures with the interrupted fin heat exchanger and the other configurations analyzed, with a maximum ΔTu of 8% in plane 4 and a radial perturbation that extends 10% of the section height more respect to the *clean* both in plane 4 and 5.

On the other side the total temperature ratio changes are inside the maximum uncertainty of 0.3% of f for the continuous fin configuration and still remain negligible for the interrupted fins, with a maximum decrease

ΔT_T = 1.4K in plane 4.

Of course these conclusions take into account only the total temperature and the turbulence maps, but the latter is the most important because allows the evaluation of the flow disturb entity introduced by the fins.

In this report was also discussed the way of functioning of the used probes in order to know the reliability of the results obtaining the acceptable level of uncertainty shown in chapter 6 of $0.1 - 0.3\%$ for the non dimensional temperature ratio and of $1 - 4.5\%$ for the turbulence.

7.2 Future works

However the analysis can be improved investigating the following points:

- the first point is to compare the total temperature and turbulence results with total pressure and flow angle data. In particular with the five holes probe it is possible to know the flow angles that can be used to construct a velocity and Mach number map with the hot wires. This map can be compared with the Pitot probe results to see if the measurements are coherent;
- the second is to introduce a continuous power supply that feeds the heat exchanger reproducing the operational turbofan conditions, also in terms of inserted heat, for a sufficient time interval. This aspect gives an higher importance to the thermocouples measurement. In the considered way of testing not relevant total temperature changes where caused by the introduction of the exchanger[1], while in the real engine a significant heat quantity inserted in the flow could increase the bypass flow energy, improving the nozzle expansion. This is an aspect that has to be evaluated in its entity;
- the third point is the temperature correction for hot wire anemometry in order to verify the error due to the temperature sensitivity of this technique;
- then could be interesting to correct the complete temperature history with the thermocouple dynamic transfer function to see the possible differences;

[1] As previously said, see section 1.2.2, the tests are *cold*, the analyzed heat exchangers are not heated up.

- and finally high frequency total temperature and pressure measurements can be done to investigate the possible energy separation in the wakes of the heat exchanger.

All these aspects increase the reliability and the accuracy of the previous achievements.

Appendix A

Matlab codes

A.1 Real OHR

```
clc
clear all
close all

R_w_c=input('Write the value of R wire at ambient temperature ...
    in ohm \');
R_ws_c=input('Write the value of R total (wire+support) at ...
    ambient temperature in ohm \');
R_cable_c=input('Write the value of R 6 m cable at ambient ...
    temperature in ohm \');
OHR=input('Write the setted Over Heat Ratio \');

%the subscript h=hot
%the subscript c=cold
%the subscript w=wire

R_TOT_h=OHR*(R_ws_c+R_cable_c);
R_w_h=R_TOT_h-R_cable_c-(R_ws_c-R_w_c);
OHR_real=R_w_h/R_w_c
```

A.2 Total temperature uncertainty

Each total temperature uncertainty, ΔT_T, can be split into a random error, ΔT_{RANDOM}, and a bias error, ΔT_{BIAS}, where:

$$\frac{\Delta T_{\text{RANDOM}}}{T} = \sqrt{\left(\frac{\Delta T_{\text{VOLTAGE}}}{T}\right)^2 + \left(\frac{\Delta T_{\text{REGRESSION}}}{T}\right)^2}$$

and

$$\frac{\Delta T_{\text{BIAS}}}{T} = \sqrt{\left(\frac{\Delta T_{\text{RESOLUTION}}}{T}\right)^2 + \left(\frac{\Delta T_{\text{PRECISION}}}{T}\right)^2}$$

The voltage uncertainty is the RMS deviation multiplied by the slope of the relative calibration curve and by a coefficient that gives the desired confidence level[1].

The regression uncertainty can be estimated with the RMS error between the calibration reference temperature data and the values calculated using the calibration line.

The resolution of the used digital acquisition system allows to neglect $\Delta T_{\text{RESOLUTION}}$[2].

At the end the precision has to be considered. During the STT calibration the bare type K thermocouples were used, so $\Delta T_{\text{PRECISION}}$ is the uncertainty that affects those thermocouples. It is evaluated considering their data regression uncertainty and the thermometer resolution.

In the following subsection the used MATLAB code is presented.

A.2.1 Code

```
%% Temperature uncertainty analysis
%before to launch this run the thermocouple analysis of plane ...
    4 acocthermal with heater off (standard test) or ...
    interrupted fins coarse (worst case); both have ref¬STT1 ...
    and calib=calib2 (done the 27/06)
%all the temperature are in Kelvin and the voltage in Volt
clc
close all
format long
```

[1] In this case the coefficient is 2 to have a 95% of confidence level.

[2] $\Delta T_{\text{RESOLUTION}} = \text{slope} \cdot V \cdot \text{span}/2^{n_{\text{bits}}}$, with span 20 volt and number of bits 16.

```
7
8  %% uncertainty due to the calibration of STT
9  %calib2 (27\06) calibration data
10 STT1_V_calib = [3.770166405; 4.249178155];
11 STT2_V_calib = [2.928255894 3.406073563 3.872685254 ...
       4.357534837 4.872981318];
12 STT4_V_calib = [3.044708046 3.520608145 3.986374034 ...
       4.472572289 4.989687597];
13 STT5_V_calib = [3.003215751 3.480164838 3.944688058 4.43087691 ...
       4.94626934];
14 T_calib_BKTs = [30.276 34.919 39.416 44.094 49.015]+273.15;
15
16 x_ref = STT1_V_calib;
17 x = [STT2_V_calib;STT4_V_calib;STT5_V_calib];
18 y_ref = T_calib_BKTs(1:2)';
19 y = repmat(T_calib_BKTs,n_heads-1,1);
20
21 a_ref = calib(1,1);
22 a = calib(2:end,1);
23 b_ref = calib(1,2);
24 b = calib(2:end,2);
25
26 T_calib = ...
       repmat(a,1,numel(x(1,:))).*x+repmat(b+273.15,1,numel(x(1,:)));
27 T_calib_ref = a_ref*x_ref+b_ref+273.15;
28 %uncertainty evaluated as a RMS value
29 ΔT_reg_ref = ...
       (sum((T_calib_ref-y_ref).^2)/(numel(T_calib_ref)-1))^0.5;
30 ΔT_reg = (sum((T_calib(:)-y(:)).^2)/(numel(T_calib)-1))^0.5;
31
32 %% Uncertainty on the temperature evaluated with the BTK
33 %data from 09_06 BKTs oil bath calibration
34 temp_eval=[25.5 0.279242073 0.268301878 0.275713619;
35 30.2    0.326182385 0.315194155 0.322708521;
36 34.9    0.376197887 0.36431505  0.372042617;
37 39.9    0.425233568 0.413665697 0.420724217;
38 44.8    0.474385953 0.463201714 0.470690935;
39 49.8    0.525322501 0.513914745 0.521087818];
40
41 T_eval=temp_eval(:,1)+273.15;
42 BKT10_V_eval=temp_eval(:,2);
43 BKT12_V_eval=temp_eval(:,3);
44 BKT13_V_eval=temp_eval(:,4);
45 %calib curves
```

```
46 BKT10_T_eval=98.7784230*BKT10_V_eval-2.1027722+273.15;
47 BKT12_T_eval=98.9293732*BKT12_V_eval-1.0425939+273.15;
48 BKT13_T_eval=99.0405379*BKT13_V_eval-1.8184009+273.15;
49
50 Tcalib_eval=[BKT10_T_eval;BKT12_T_eval;BKT13_T_eval];
51 T_eval=repmat(T_eval,3,1);
52
53 ΔT_eval_BKT10 = (sum((Tcalib_eval(1:6)-T_eval(1:6)).^2)/5)^0.5;
54 ΔT_eval_BKT12 = (sum((Tcalib_eval(7:12)-T_eval(7:12)).^2)/5)^0.5;
55 ΔT_eval_BKT13 = ...
       (sum((Tcalib_eval(13:end)-T_eval(13:end)).^2)/5)^0.5;
56
57 ΔT_eval_random = ...
       (sum((Tcalib_eval-T_eval).^2)/(numel(Tcalib_eval)-1))^0.5;
58 %termometer resolution
59 ΔT_eval_bias = 0.05;
60
61 ΔT_eval = ΔT_eval_random+ΔT_eval_bias;
62 ΔT_eval_ref = ΔT_eval;
63
64 %% Δ T random due to voltage uncertainty
65 std_probe_val_filtered = ones(n_points,size(probe_val_filt,2));
66 std_inlet_probe_val_filtered = ones(n_points);
67 for k1=1:n_points
68     std_probe_val_filtered(k1,:) = ...
          std(probe_val_filt(f_s*(k1-1)+1:f_s*k1,:)+273.15);
69     std_inlet_probe_val_filtered(k1) = ...
          std(ref_probe_val_filt(f_s*(k1-1)+1:f_s*k1)+273.15);
70 end
71 ΔT_V_1 = 2*std_probe_val_filtered(:,1);
72 ΔT_V_2 = 2*std_probe_val_filtered(:,2);
73 ΔT_V_4 = 2*std_probe_val_filtered(:,3);
74 ΔT_V_5 = 2*std_probe_val_filtered(:,4);
75 ΔT_V_inlet = 2*std_inlet_probe_val_filtered';
76 ΔT_V_ref = ΔT_V_1;
77
78 %% Total temperature finale error
79 ΔT_random_ref = (ΔT_reg_ref^2+ΔT_V_ref.^2).^0.5;
80 ΔT_random_1 = (ΔT_reg^2+ΔT_V_1.^2).^0.5;
81 ΔT_random_2 = (ΔT_reg^2+ΔT_V_2.^2).^0.5;
82 ΔT_random_4 = (ΔT_reg^2+ΔT_V_4.^2).^0.5;
83 ΔT_random_5 = (ΔT_reg^2+ΔT_V_5.^2).^0.5;
84 ΔT_random = [ΔT_random_1;ΔT_random_2;ΔT_random_4;ΔT_random_5];
85 ΔT_bias = ΔT_eval;
```

```
86 ΔT_bias_ref = ΔT_eval_ref;
87 ΔT = ΔT_random+ΔT_bias;
88 ΔT_ref = ΔT_random_ref+ΔT_bias_ref;
89
90 %% Ratio final error evaluated with the perturbation method
91 T_ref = Tref3;
92 T = Ta_woff;
93 ΔT_ref = repmat(ΔT_ref,n_heads,1);
94 Δf = ((ΔT./T_ref).^2+((-T.*ΔT_ref)./T_ref.^2).^2).^0.5;
```

A.3 Turbulence uncertainty

```
1  %% Uncertainty analysis
2  clc
3  clear all
4  close all
5  format long
6
7  %% Turbulence
8
9  %loading data from Laura's hot wire 5 (red) calibration
10 gamma=1.4;
11 %atmospheric pressure in the calibration day [Pa]
12 p_s=100853.9302;
13 %calibration coefficien to be compared with the regression results
14 calib = [0.031300 -0.517478 4.092685 9.617225 30.227146];
15
16 %load the calibration data (total pressure [gauge pressure in ...
       Pa]; total temperature [K]; calculated velocity [m/s]; hot ...
       wire voltage [V])
17 data=xlsread('uncertainty.xls',1,'A3:D39');
18 p_t=data(:,1);
19 p_t=p_t+p_s;
20 T_t=data(:,2);
21 u=data(:,3);
22 probe_V = data(:,4);
23
24 %regression
25 probe_V=[ones(numel(probe_V),1) probe_V probe_V.^2 probe_V.^3 ...
       probe_V.^4];
26 [reg_u,reg_int_u] = regress(u,probe_V);
27 c1 = reg_u(1);
28 c2 = reg_u(2);
```

```
29 c3 = reg_u(3);
30 c4 = reg_u(4);
31 c5 = reg_u(5);
32 calib2 = [c5 c4 c3 c2 c1];
33
34 %typical sensor uncertainty input values @ 2sigma
35 Δ_T_t = 0.1; %[K]
36 Δ_p_t = data(:,1)/100; %[Pa] 1\% of the gauge pressure
37 Δ_p_s = 20; %[Pa]
38
39 %uncertainty for polynomial regression
40 u_i = polyval(calib2,probe_V(:,2));
41 %uncertainty evaluated as a RMS value
42 Δ_u_reg = (sum((u-u_i).^2)/numel(u)).^0.5;
43
44 %uncertainty due to the voltage uncertainty
45 %typical standard deviation for our measurements
46 Δ_V = 0.025;
47 %to have a confidence level of 95%
48 Δ_V = Δ_V*2;
49 %uncertainty evaluated with the partial derivatives
50 Δ_u_V = ((c2+2*c3*probe_V(:,2)+3*c4*probe_V(:,2).^2+...
51     4*c5*probe_V(:,2).^3).^2*Δ_V^2).^0.5;
52 %uncertainty evaluated with the perturbation ...
       method=((u(V)-u(V+dV))^2)^0.5
53 Δ_u_V2 = ((u_i-polyval(calib2,probe_V(:,2)+Δ_V)).^2).^0.5;
54 % NOTE: the 2 methods gives equivalent results
55
56 %uncertainty in evaluating u during the calibration
57 Δ_u_calib = (u/2).*((T_t/Δ_T_t).^(-2)+(((1/gamma)*(1-...
58     (p_t/p_s).^((gamma-1)/gamma)).^(-1)).^2).*((Δ_p_t./p_t).^2+...
59     (Δ_p_s/p_s)^2)).^0.5;
60
61 %it would be possible to evaluate the uncertainty on the ...
       velocity due to the calibration uncertainty evaluating ...
       different polynomial coefficients sets (c1,...,c5) and ...
       (c1_prime,...,c5_prime) using respectively u and ...
       u+Δ_u_calib and then evaluating ...
       ((u(c1,...,c5)-u(c1_prime,...,c5_prime))^2)^0.5 and sum it ...
       with the total Δ u percent
62 u_prime = u+Δ_u_calib;
63 [reg_u_prime,reg_int_u_prime] = regress(u_prime,probe_V);
64 c1_prime = reg_u_prime(1);
65 c2_prime = reg_u_prime(2);
```

```
66 c3_prime = reg_u_prime(3);
67 c4_prime = reg_u_prime(4);
68 c5_prime = reg_u_prime(5);
69 calib2_prime = [c5_prime c4_prime c3_prime c2_prime c1_prime];
70 u_i_prime = polyval(calib2_prime,probe_V(:,2));
71 %uncertainty evaluated with the perturbation method
72 Δ_u_4calib = ((u_i-u_i_prime).^2).^0.5;
73
74 %total velocity uncertainty
75 Δ_u_tot_non_dimensional = ((Δ_u_V2.^2+Δ_u_reg.^2).^0.5)./u_i;
76 %including the calibration uncertainty
77 Δ_u_tot_non_dimensional2 = ...
       ((Δ_u_V2.^2+Δ_u_reg.^2+Δ_u_4calib.^2).^0.5)./u_i;
78
79 %turbulence uncertainty (it is possible to demonstrate that ...
       the considered uncertainties spead in the same way both to ...
       u_mean both to u_RMS, see the paper of the uncertainties ...
       in the hot wire, so Δ_u_tot/u = Δ_u_mean_tot/u_mean = Δ...
       _u_RMS_tot/u_RMS. This means that Δ_Tu_non_dimensional = Δ...
       _Tu/Tu is equal to  Δ_u_tot_non_dimensional*(2)^0.5
80 Δ_Tu_non_dimensional = Δ_u_tot_non_dimensional2*(2)^0.5;
81
82 % DEMONSTRATION:
83 %Δ_Tu = ...
       ((d(Tu)/d(u_RMS)*Δ_u_RMS)^2+(d(Tu)/d(u_mean)*Δ_u_mean)^2)^0.5
84 %WHERE
85 %Tu=u_RMS/u_mean
86 %SO
87 %(d(Tu)/d(u_RMS)=1/u_mean
88 %(d(Tu)/d(u_mean)=-u_RMS/(u_mean)^2
89 %SUBSTITUTING AND CONSIDERING THAT Δ_u_mean/u_mean = Δ_u_RMS/u_RMS
90 %Δ_Tu=Δ_u_RMS/U_rms*((u_RMS/u_mean)^2+(u_RMS/u_mean)^2)^0.5 =...
91 %Δ_u_RMS/U_rms*(2Tu^2)^0.5=Tu*Δ_u_tot_non_dimensional*(2)^0.5
```

Bibliography

[1] T. Arts, H. Boerrigter, J.M. Buchlin, M. Carbonaro, G. Degrez, R. Dénos, D. Fletcher, D. Olivari, M.L. Riethmuller, R.A. Van den Braembussche, *Measurement techniques in fluid dynamics*, 2001.

[2] L. Villafañe, *Aerothermal Analysis and Characterization of Fine Wire Thermocouple Probes.*

[3] L. Villafañe, G. Paniagua, M. Kaya, D. Bajusz, S. Hiernaux, *Development of a transonic wind tunnel to investigate engine bypass flow heat exchangers*, 2011.

[4] L. Villafañe, T. Yasay, G. Paniagua, G. Bonfanti, *Development of Experimental Techniques for the Characterization of Helicoidal Fin Arrays in Transonic Flow Conditions.*

[5] ASTM manual, *MANUAL ON THE USE OF THERMOCOUPLES IN TEMPERATURE MEASUREMENT.*

[6] G. Paniagua, R. Dénos, M. Oropesa, *Thermocouple probes for accurate temperature measurements in short duration facilities*, 2002.

[7] M. Tagawa, T. Shimoji, Y. Ohta, *A two-thermocouple probe technique for estimating thermocouple time constants in flows with combustion: In situ parameter identification of a first-order lag system*, 1998.

[8] G. Recktenwald, *Uncertainty Estimation and Calculation*, 2006.

[9] J. W. Cooley and J. Tukey, *An algorithm for the machine calculation of complex Fourier series*, 1965.

[10] F. Liu, W.A. Sirignano, *Turbojet and turbofan engine performance increases through turbine burners*, 2001.

[11] Rolls-Royce plc, *The Jet Engine*, 2005.

[12] Rolls-Royce plc, *Gas turbine technology, introduction to a jet engine*, 2007.

[13] F. Paganucci, *Aircraft Engines Course Notes*, 2008.

[14] T. Yasa, G. Paniagua and R. Dénos, *Application of hot-wire anemometry in a blow-down turbine facility*, 2006.

[15] T. Yasa, G. Paniagua and R. Dénos, *Hot-wire anemometry for non-isothermal flows and effect of aging of the sensor wire*, 2005.

[16] H. H. Bruun, *Hot-wire anemometry, principles and signal analysis*, 1995.

[17] S. Acarer, *Hot-wire anemometry in two dimensional high speed flow*, 2011.

[18] Dantec Dynamics A/S, *Dantec manual*, 2007.

[19] F. E. Jørgensen, *How to measure turbulence with hot-wire anemometers - a practical guide*, 2002.

[20] W. P. Bennet, A. Rona, J. R. Ackerman and J. P. Gostelow, *Experimental and numerical study of the non-uniform total temperature in a turbulent mach 0.6 vortex street*, 2003.

[21] J. P. Gostelow and W. E. Carscallen, *Investigations of Eckert-Weise energy separation in the wakes of turbine blades and circular cylinders*, 2010.

[22] N. Erriu, N. Mandas and P.Puddu, *Alcune considerazioni sulla valutazione dell'incertezza nelle misure con anemometro a filo caldo*, 2001.